

**OBSERVATIONS OF HIGHLY OXIDISED  
MOLECULES AND PARTICLE NUCLEATION  
IN THE ATMOSPHERE OF BEIJING**

**James Brean<sup>1</sup>, Roy M. Harrison<sup>1,\*†</sup>, Zongbo Shi<sup>1</sup>  
David C.S. Beddows<sup>1</sup>, W. Joe F. Acton<sup>2</sup>  
C. Nicholas Hewitt<sup>2</sup>, Freya A. Squires<sup>3</sup> and James Lee<sup>3</sup>**

**<sup>1</sup>Division of Environmental Health and Risk Management,  
School of Geography, Earth and Environmental Sciences  
University of Birmingham  
Edgbaston, Birmingham B15 2TT  
United Kingdom**

**<sup>2</sup>Lancaster Environment Centre  
Lancaster University, Lancaster LA1 4YQ  
United Kingdom**

**<sup>3</sup>National Centre for Atmospheric Science  
Wolfson Atmospheric Chemistry Laboratory  
University of York, York YO10 5DD  
United Kingdom**

---

\* To whom correspondence should be addressed.

Tele: +44 121 414 3494; Fax: +44 121 414 3709; Email: r.m.harrison@bham.ac.uk

†Also at: Department of Environmental Sciences / Center of Excellence in Environmental Studies, King Abdulaziz University, PO Box 80203, Jeddah, 21589, Saudi Arabia

## 25    **ABSTRACT**

26    Particle nucleation is one of the main sources of atmospheric particulate matter by number, with new  
27    particles having great relevance for human health and climate. Highly oxidised multifunctional  
28    organic molecules (HOMs) have been recently identified as key constituents in the growth, and,  
29    sometimes, in initial formation of new particles. While there have been many studies of HOMs in  
30    atmospheric chambers, flow tubes and clean environments, analyses of data from polluted  
31    environments are scarce. Here, measurements of HOMs and particle size distributions down to small  
32    molecular clusters are presented alongside volatile organic compounds (VOC) and trace gas data from  
33    a campaign in June 2017, in Beijing. Many gas phase HOMs have been characterised and their  
34    temporal trends and behaviours analysed in the context of new particle formation. The HOMs  
35    identified have a comparable degree of oxidation to those seen in other, cleaner, environments, likely  
36    due to an interplay between the higher temperatures facilitating rapid hydrogen abstractions and the  
37    higher concentrations of  $\text{NO}_x$  and other  $\text{RO}_2^\cdot$  terminators ending the autoxidation sequence more  
38    rapidly. Our data indicate that alkylbenzenes, monoterpenes, and isoprene are important precursor  
39    VOCs for HOMs in Beijing. Many of the  $\text{C}_5$  and  $\text{C}_{10}$  compounds derived from isoprene and  
40    monoterpenes have a slightly greater degree of average oxidation state of carbon compared to those  
41    from other precursors. Most HOMs except for large dimers have daytime peak concentrations,  
42    indicating the importance of  $\text{OH}^\cdot$  chemistry in the formation of HOMs, as  $\text{O}_3$  tends to be lower on  
43    days with higher HOM concentrations ; similarly, VOC concentrations are lower on the days with  
44    higher HOM concentrations. The daytime peaks of HOMs coincide with the growth of freshly formed  
45    new particles, and their initial formation coincides with the peak in sulfuric acid vapours, suggesting  
46    that the nucleation process is sulfuric acid-dependent, with HOMs contributing to subsequent particle  
47    growth.

48

49

## 1. INTRODUCTION

Atmospheric particle nucleation, or the formation of solid or liquid particles from vapour phase precursors is one of the dominant sources of global aerosol by number, with primary emissions typically dominating the mass loadings (Tomasi et al., 2016). New particle formation (NPF) or the secondary formation of fresh particles is a two-step process comprising of initial homogeneous nucleation of thermodynamically stable clusters and their subsequent growth. The rate of growth needs be fast enough to out-compete the loss of these particles by coagulation and condensation processes in order for the new particles to grow, and hence NPF is a function of the competition between source and sink (Gong et al., 2010). New particle formation has been shown to occur across a wide range of environments (Kulmala et al., 2005). The high particle load in urban environments was thought to suppress new particle formation until measurements in the early 2000s (McMurry et al., 2000; Shi et al., 2001; Alam et al., 2003), with frequent occurrences observed even in the most polluted urban centres. NPF events in Beijing occur on about 40% of days annually, with the highest rates in the spring (Wu et al., 2007, 2008; Wang et al., 2016). Chu et al. (2019) review many studies of NPF which have taken place in China and highlight the need for long-term observations and mechanistic studies.

NPF can lead to [the](#) production of cloud condensation nuclei (CCN) (Wiedensohler et al., 2009; Yu and Luo, 2009; Yue et al., 2011; Kerminen et al., 2012) which influences the radiative atmospheric forcing (Penner et al., 2011). A high particle count, such as that caused by nucleation events, has been shown to precede haze events in environments such as Beijing (Guo et al., 2014). These events are detrimental to health and quality of life. The sub-100 nm fraction of particles to which new particle formation contributes to is often referred to as the ultrafine fraction. Ultrafine particles (UFPs) pose risks to human health due to their high number concentration. UFPs exhibit gas-like behaviour and enter all parts of the lung before penetrating into the bloodstream (Miller et al., 2017). They can initiate inflammation via oxidative stress responses, progressing conditions such as

76 atherosclerosis and initiating cardiovascular responses such as hypertension through to myocardial  
77 infarction (Delfino et al., 2005; Brook et al., 2010).

78

79 Highly oxidised multifunctional molecules (HOMs), organic molecules with O:C ratios >0.6, are  
80 the result of atmospheric autoxidation and have recently been subject to much investigation, in part  
81 because the extremely low volatilities arising from their high O:C ratios favour their condensation  
82 into the particulate phase. HOMs are most well characterised as the product of oxidation of the  
83 biogenic monoterpene compound  $\alpha$ -pinene (Riccobono et al., 2014; Tröstl et al., 2016; Bianchi et  
84 al., 2017). Although globally, biogenic volatile organic compound (BVOC) concentrations far  
85 exceed anthropogenic volatile organic compound (AVOC) concentrations, in the urban environment  
86 the anthropogenic fraction is far more significant. Formation of HOMs from aromatic compounds  
87 has been demonstrated in laboratory studies and these have been hypothesised to be large drivers of  
88 NPF in urban environments (Wang et al., 2017; Molteni et al., 2018; Qi et al., 2018). The formation  
89 of HOMs through autoxidation processes begins with the reaction of VOCs with OH, O<sub>3</sub> or NO<sub>3</sub>;  
90 formation of a peroxy radical (RO<sub>2</sub>) is followed by rapid O<sub>2</sub> additions and intra-molecular hydrogen  
91 abstractions (Jokinen et al., 2014; Rissanen et al., 2014; Kurtén et al., 2015). Furthermore,  
92 generation of oligomers from stabilised Criegee intermediates arising from short chain alkenes has  
93 been hypothesised as a contributor of Extremely Low Volatility Organic Compounds (ELVOCs)  
94 and Low Volatility Organic Compounds (LVOCs) (Zhao et al., 2015). The low volatilities of these  
95 molecules arise from their numerous oxygen-containing functionalities, and this allows them to  
96 make a significant contribution to early stage particle growth where other species cannot due to the  
97 Kelvin effect (Tröstl et al., 2016), although the contribution of HOMs to the initial molecular  
98 clusters is still debated (Kurtén et al., 2016; Elm et al., 2017; Myllys et al., 2017).

99

100 Recent technological advances have facilitated insights into the very first steps of nucleation which  
101 were previously unseen, with mass spectrometric techniques such as the Atmospheric Pressure

Interface Time of Flight Mass Spectrometer (APi-ToF) and its chemical ionisation counterpart (CI-APi-ToF) allowing for high mass and time resolution measurements of low volatility compounds and molecular clusters. Diethylene glycol based particle counters, such as the Particle Size Magnifier (PSM) allow for measurements of particle size distributions down to the smallest molecular clusters nearing 1 nm. Recent chamber studies have elucidated the contribution of individual species to particle nucleation, ammonia and amines greatly enhancing the rate of sulfuric acid nucleation (Kirkby et al., 2011; Almeida et al., 2013). In these studies, HOMs have been identified, formed through autoxidation mechanisms (Schobesberger et al., 2013; Riccobono et al., 2014; Ehn et al., 2014). These are key to early particle growth (Tröstl et al., 2016) and can nucleate even in the absence of sulfuric acid in chambers (Kirkby et al., 2016) and in the free troposphere (Rose et al., 2018). In this paper, we report the results of HOM and particle size measurements during a summer campaign in Beijing, China.

114

## 115 **2. DATA AND METHODS**

### 116 **2.1. Sampling Site**

117 Sampling was performed as part of the Air Pollution and Human Health in a Developing Megacity  
118 (APHH-Beijing) campaign, a large international collaborative project examining emissions,  
119 processes and health effects of air pollution. For a comprehensive overview of the programme, see  
120 Shi et al. (2019). All sampling was conducted across a one month period at the Institute for  
121 Atmospheric Physics (IAP), Chinese Academy of Sciences, Beijing (39°58.53'N, 116°22.69'E).  
122 The sampling was conducted from a shipping container, with sampling inlets 1-2 metres above  
123 ground level, the nearest road being 30 metres away. Meteorological parameters (wind speed, wind  
124 direction, relative humidity (RH) and temperature) were measured at the IAP meteorological tower,  
125 20 metres away from the sampling site, 30 metres from the nearest road at a height of 120 metres.  
126 Data was continuously taken from the CI-API-ToF during a two week period, but due to data losses

127 only five days of data is presented here. Particle size distribution measurements were taken during a  
128 33 day period from 24/05/2017 – 26/06/2017.

129

## 130 **2.2 Chemical Ionisation Atmospheric Pressure Interface Time of Flight Mass**

### 131 **Spectrometry**

132 The Aerodyne Nitrate Chemical Ionisation Atmospheric Pressure Interface Time of Flight Mass  
133 Spectrometer (CI-APi-ToF) was used to make measurements of neutral oxidised organic  
134 compounds, sulfuric acid and their molecular clusters at high time resolution with high resolving  
135 power. The ionization system charges molecules by adduct formation, such as in the case of organic  
136 compounds with two or more hydrogen bond donor groups (Hytinen et al., 2015), or proton  
137 transfer in the case of strong acids like sulfuric acid. Hydroxyl or hydroperoxyl functionalities are  
138 both common hydrogen bond donating groups, with hydroperoxyl being the more efficient  
139 hydrogen bond donor (Møller et al., 2017). This instrument has been explained in great detail  
140 elsewhere (Junninen et al., 2010; Jokinen et al., 2012), but briefly the front end consists of a  
141 chemical ionisation system where a 10 LPM sample flow is drawn in through the 1 metre length 1”  
142 OD stainless steel tubing opening. A secondary flow was run parallel and concentric to this sample  
143 flow, rendering the reaction chamber effectively wall-less. A 3 SCCM flow of a carrier gas (N<sub>2</sub>) is  
144 passed over a reservoir of liquid HNO<sub>3</sub>, entraining vapour which is subsequently ionised to NO<sub>3</sub><sup>-</sup> via  
145 an X-ray source. This flow is then guided into the sample flow. . The nitrate ions will then charge  
146 molecules either by clustering or proton transfer. The mixed flows travelling at 10 LPM enter the  
147 critical orifice at the front end of the instrument at 0.8 LPM and are guided through a series of  
148 differentially pumped chambers before reaching the ToF analyser. Two of these chambers contain  
149 quadrupoles which can be used to select greater sensitivity for certain mass ranges, and the voltages  
150 across each individual chamber can be tuned to maximise sensitivity and resolution for ions of  
151 interest. Mass spectra are taken at a frequency of 20 kHz but are recorded at a rate of 1 Hz. All data  
152 analysis was carried out in the *Tofware* package in *Igor Pro 6* (Tofwerk AG, Switzerland). A seven

point mass calibration was performed for every minute of data, and all data was normalised to  
 signal at 62, 80 and 125  $m/Q$  to account for fluctuations in ion signal, these masses representing  
 $\text{NO}_3^-$ ,  $\text{H}_2\text{ONO}_3^-$  and  $\text{HNO}_3\text{NO}_3^-$  respectively. ~~The resultant normalised counts have been multiplied  
 by  $10^5$  so magnitudes are similar to the original count rates.~~ Typical values for calibration  
 coefficients range from  $10^9$ - $10^{10}$  molecules  $\text{cm}^{-3}$  from these normalised data (Kürten et al., 2012),  
 producing peak sulfuric acid concentrations in the range of  $10^6$  molecules  $\text{cm}^{-3}$ . From the very  
 limited periods with simultaneous data for  $\text{SO}_2$ , OH radical and condensation sink, it was possible  
 to calculate  $\text{H}_2\text{SO}_4$  concentrations of  $10^3$  to  $10^5$  molec  $\text{cm}^{-3}$ , in which range the calibration constant  
 was  $7.0 \pm 1.6 \times 10^8 \text{ cm}^{-3}$  which fits well with that expected for this concentration range (Kürten et  
 al., 2012). The nitrate-water cluster is included as the presence of many nitrate-water clusters of the  
 general formula  $(\text{H}_2\text{O})_x(\text{HNO}_3)_y\text{NO}_3^-$  were found, where  $x = (1, 2, 3 \dots 20)$  and  $y = (0, 1)$ . No  
 sensitivity calibration was performed for these measurements, and so all values are reported in  
 normalised signal intensity. Due to the high resolving power of the CI-APi-ToF system (mass  
 resolution of 3500  $m/\text{dm}$  and mass accuracy of 20 ppm at 288  $m/Q$ ), multiple peaks can be fit at the  
 same unit mass and their molecular formulae assigned. These peaks follow the general formula  
 $\text{C}_x\text{H}_y\text{O}_z\text{N}_w$  where  $x = 2\text{--}20$ ,  $y = 2\text{--}32$ ,  $z = 4\text{--}16$  and  $w = 0\text{--}2$ , spanning from small organic acids like  
 oxalic and malonic acid through to large dimers of oxidised monoterpene  $\text{RO}_2^-$  radicals such as  
 $\text{C}_{20}\text{H}_{31}\text{O}_9\text{N}$ . ~~The~~ Beyond 500  $m/Q$ , peak fitting and assignment of compositions becomes  
 problematic as signal decreases, mass accuracy decreases, and the total number of chemical  
 compositions increases, so peaks above the  $\text{C}_{20}$  region have not been assigned, and a number of  
 peaks have been unassigned due to this uncertainty (Cubison and Jimenez, 2015). As proton transfer  
 mostly happens with acids, and nearly all HOM molecules will be charged by adduct formation it is  
 possible to infer the uncharged formula; therefore all HOMs from here onwards will be listed as  
 their uncharged form.

### 2.3. Size Distribution Measurements

Two Scanning Mobility Particle Sizer (SMPS) instruments measured particle size distributions at 15 minute time resolution, one LongSMPS (TSI 3080 EC, 3082 Long DMA, 3775 CPC, TSI, USA) and one NanoSMPS (3082 EC, 3082 Nano DMA, 3776 CPC, TSI, USA) measuring the ranges 14-615 nm and 4-65 nm respectively. A Particle Size Magnifier (A10, Airmodus, FN) linked to a CPC (3775, TSI, USA) measured the sub-3 nm size fraction. The PSM was run in stepping mode, operating at four different saturator flows to vary the lowest size cut-off of particles that it will grow (this cut-off is technically a point of 50% detection efficiency) of <1.30, 1.36, 1.67 and 2.01 nm. The instrument switched between saturator flows per 2.5 minutes, giving a sub-2.01 nm size distribution every 10 minutes. The data was treated with a moving average filter to account for jumps in total particle count, and due to the similar behaviour of the two upper and two lower size cuts, these have been averaged to two size cuts at 1.30 and 1.84 nm.

### 2.4. Calculations

The condensation sink (CS) was calculated from the size distribution data as follows:

$$CS = 4\pi D \sum_{d'_p} \beta_{m,d'_p} d'_p N_{d'_p} \quad (1)$$

where D is the diffusion coefficient of the diffusing vapour (assumed sulfuric acid),  $\beta_m$  is a transition regime correction (Kulmala et al., 2012),  $d'_p$  is particle diameter, and  $N_{d'_p}$  is the number of particles at diameter  $d'_p$ .

### 2.5. Other Measurements

Measurements of the classical air pollutants were measured on the same site, and have been reported in the campaign overview paper (Shi et al., 2019). SO<sub>2</sub> was measured using a 43i SO<sub>2</sub> analyser (ThermoFisher Scientific, USA), O<sub>3</sub> with a 49i O<sub>3</sub> analyser (ThermoFisher Scientific,



204 USA) and NO<sub>x</sub> with a 42i-TL Trace NO<sub>x</sub> analyser (ThermoFisher Scientific, USA), and a T500U  
205 CAPS NO<sub>2</sub> analyser (Teledyne API, USA). VOC mixing ratios were measured using a Proton  
206 Transfer Reaction-Time of Flight-Mass Spectrometer (PTR-ToF 2000, Ionicon, Austria).

207

## 208 **3. RESULTS AND DISCUSSION**

### 209 **3.1. Characteristics of Sampling Period**

210 A total of five days of CI-API-ToF data were collected successfully, from 2017/06/21 midday  
211 through 2017/06/26 midday. New particle formation events were observed on 24<sup>th</sup> June in the late  
212 afternoon and 25<sup>th</sup> June at midday. Some nighttime formation of molecular clusters was seen  
213 earlier in the campaign, as were several peaks to the 1.5 – 100 nm size range, likely from pollutant  
214 plumes containing freshly nucleating condensable materials. The trace gases, O<sub>3</sub>, SO<sub>2</sub>, NO and NO<sub>2</sub>  
215 are plotted in the Figure S1. O<sub>3</sub> shows mid-afternoon peaks, around ~120 ppb on the first two days  
216 of the campaign, and 50-70 ppb for the latter days. SO<sub>2</sub> shows a large peak, reaching 4 ppb on 22/06  
217 but <1 ppb for the rest of campaign. NO shows strong mid-morning rush hour related peaks,  
218 declining towards midday due to being rapidly consumed by O<sub>3</sub>. NO<sub>2</sub> shows large traffic related  
219 peaks. The sulfuric acid signal across this period as measured by NO<sub>3</sub><sup>-</sup> CI-API-ToF showed strong  
220 midday peaks, with signal highest on 24/06/2017 and 25/06/2017. The meteorological data are  
221 shown in Figure S2 alongside condensation sink (CS). The conditions were generally warm and  
222 humid, with temperature reaching its maximum on 25/06/2017, with a peak hourly temperature of  
223 31°C. High temperatures were seen on 21/06 and 24/06 also, of 30°C and 26°C respectively.

224

### 225 **3.2. Gas Phase HOM Chemistry**

#### 226 **3.2.1. Bulk chemical properties**

227 For the peaks that have had chemical formulae assigned, oxidation state of carbon, or *OS<sub>c</sub>*, can be  
228 used to describe their bulk oxidation chemistry. *OS<sub>c</sub>* is defined as (Kroll et al., 2011)

229

$$OSc = (2 \times O:C) - H:C \quad (2)$$

230  
231  
232  
233  
234  
235  
236  
237  
238  
239  
240  
241  
242  
243  
244  
245  
246  
247  
248  
249  
250  
251

This does not account for the presence of nitrate ester groups, which has been accounted for previously by subtracting five times the N:C ratio (Massoli et al., 2018), under the assumption that all nitrogen containing functionality is in the form of nitrate ester (RONO<sub>2</sub>) groups. In Beijing, multiple sources of nitrate-containing organic compounds are seen, in the forms of amines, nitriles and heterocycles. The variation of oxidation state with carbon number ( $C_n$ ) without correction for nitrate esters is plotted in Figure 1. The average oxidation state of carbon in this dataset tends to decrease with an increase to  $C_n$ , highest where  $C_n = 5$ , attributable both to high O:C and peak area for the peak assigned to C<sub>5</sub>H<sub>10</sub>N<sub>2</sub>O<sub>8</sub> at  $m/Q$  288.  $C_n = 5$  also shows the greatest distribution of oxidation states, likely due to the high ambient concentration of isoprene and therefore its many oxidation products being of high enough signal for many well resolved peaks to be seen in this dataset. It is worth noting that some of the ions plotted here may not form through peroxy radical autoxidation, such as C<sub>5</sub>H<sub>10</sub>N<sub>2</sub>O<sub>8</sub>, which may be a second-generation oxidation product of isoprene under high NO<sub>x</sub> (Lee et al., 2016).  $C_n = 10$  and 15 also see a small increase to average oxidation number compared to their neighbours. The lower oxidation state of the larger products is likely a function of two things. First and foremost, any autoxidation mechanism must undergo more steps in order for a larger molecule to reach an equivalent O:C ratio with a smaller one, and the equivalent O:C ratio is ultimately less likely to be reached before the radical is terminated (Massoli et al., 2018). Secondly, the lower vapour pressures of these larger products will lead to their partitioning into the condensed phase more readily than the smaller, thus they are more rapidly lost (Mutzel et al., 2015).

252  
253  
254  
255

The degrees of OSc observed here are similar to those seen in other environments such as during the SOAS campaign in 2013 in southern United States, characterised by low NO/NO<sub>2</sub> and high temperatures, where campaign averages of 0.3 ppb, 0.4-0.5 ppb, and 25°C respectively were

256 measured, although an additional parameter to account for nitrogen containing VOCs is included in  
257 the calculation (Massoli et al., 2018). The  $OS_c$  observed in Beijing is also higher than that seen in  
258 the boreal forest environment of Hyytiälä, despite extremely low  $NO_x$  concentrations, likely due to  
259 low temperature conditions dominating in those conditions (Schobesberger et al., 2013). These  
260 relatively similar degrees of oxidation to those seen in other, cleaner, environments are likely due to  
261 an interplay between the higher temperatures facilitating rapid hydrogen abstractions (Crounse et  
262 al., 2013; Quéléver et al., ~~2018~~[2019](#)) and the higher concentrations of  $NO_x$ ,  $HO_2$ , and other  $RO_2$   
263 molecules terminating the autoxidation sequence more efficiently (Praske et al., 2018, Rissanen,  
264 2018, Garmash et al., 2019).

265  
266 A mass defect plot is shown in Figure 2, which shows nominal mass plotted against mass defect for  
267 all peaks in this dataset. Mass defect is defined as the ion mass minus integer mass. This is shown  
268 for two separate daytime periods, one where nucleation was not occurring and HOM concentrations  
269 are lower (10:30 – 12:00 23/06/2017) and one where nucleation was occurring under high HOM  
270 concentrations (10:30 – 12:00 25/06/2017). The band of lower mass defect is characterised by a  
271 number of large peaks with high signal, for example, at  $m/Q$  436 the ion  $(C_2H_7N)_2(H_2SO_4)_2HSO_4^-$ .  
272 The upper component of the mass defect is dominated by organic compounds, the upper end of  
273 more positive mass defect is occupied by molecules with more  $^1H$  (mass defect 7.825 mDa) and  $^{14}N$   
274 (mass defect 3.074 mDa). The end of less positive mass defect has lower  $^1H$  and more  $^{16}O$  (mass  
275 defect -5.085 mDa); alternatively put, the mass defect reflects the variation in  $OS_c$ . The organic  
276 components with more positive mass defects will be more volatile than their lower mass defect  
277 counterparts as they will contain fewer oxygen functionalities (Tröstl et al., 2016, Stolzenburg et al.,  
278 2018). These higher volatility products may still contribute to larger size particle growth. The more  
279 negative mass defect components will be those of greater O:C and therefore lower volatility,  
280 LVOCs, and the yet larger and more oxidised components, ELVOCs (Tröstl et al., 2016). During  
281 the nucleation period, the signal intensity for the species in the upper band of more negative mass

282 defect have the most marked increase in concentration, with significantly less difference >500 m/Q.  
283 This region 200-400 m/Q will contain most of the  $\geq C_5$  monomer HOMs seen in this dataset.  
284

### 285 3.2.2. Diurnal trends of HOMs

286 Temporal trends of HOMs in the urban atmosphere can reveal their sources and behaviour in the  
287 atmosphere. Most of the HOM species peak in the daytime. These species all follow a similar  
288 diurnal trend, as shown in Figure 3. Both the concentrations of  $O_3$  and  $OH^\cdot$  are high during the  
289 summer period in Beijing (although the nitrate chemical ionisation technique is not sensitive to all  
290  $OH^\cdot$  oxidation products (Berndt et al., 2015)). Figure S1 shows the time series of concentrations of  
291  $NO$  which is considered a dominant peroxy radical terminator of particular importance in the  
292 polluted urban environment (Khan et al., 2015). Radicals such as  $HO_2^\cdot$  and  $RO_2^\cdot$  also typically peak  
293 during daytime. The HOM components peaking in the daytime are presumed to be the oxidation  
294 products of a mixture of anthropogenic and biogenic components, such as alkylbenzenes,  
295 monoterpenes and isoprene. The oxidation of monoterpenes, specifically the monoterpene  $\alpha$ -pinene,  
296 has been the subject of extensive study recently, with the  $O_3$ -initiated autoxidation sequence being  
297 the best characterised (Ehn et al., 2014; Jokinen et al., 2014; Kurtén et al., 2015; Kirkby et al.,  
298 2016); ozonolysis of  $\alpha$ -pinene opens the ring structure and produces a  $RO_2^\cdot$  radical (Kirkby et al.,  
299 2016). In the case of aromatics,  $OH^\cdot$  addition to the ring and the subsequently formed bicyclic  
300 peroxy radical is the basis for the autooxidation of compounds such as xylenes and  
301 trimethylbenzenes (Molteni et al., 2018; Wu et al., 2017).

302  
303 The identified compounds have been roughly separated into several categories, each of these plotted  
304 in Figure 3. Figure 3 shows the separation of components into non-nitrogen containing HOMs, and  
305 nitrogen containing HOMs, or organonitrates (ONs). The ON signal is much higher than that of the  
306 HOM, attributable in part to a few ions of high signal, such as the isoprene organonitrate  
307  $C_5H_{10}N_2O_8$ . A few similar structural formulae are seen ( $C_5H_{10}N_2O_6$ ,  $C_5H_{11}NO_6$ ,  $C_5H_{11}NO_7$ , etc),

308 some of which have been identified as important gas phase oxidation products of isoprene under  
 309 high  $\text{NO}_x$  conditions (Xiong et al., 2015), and their contribution to SOA has been explored  
 310 previously (Lee et al., 2016). A high nitrophenol signal is also seen,  $\text{C}_6\text{H}_5\text{NO}_3$ . The signal for HOM  
 311 compounds is less dominated by a few large ions. The prevalence of ON compounds points towards  
 312 the important role of  $\text{NO}_x$  as a peroxy radical terminator, with the probability for the  $\text{RO}_2^\cdot + \text{NO}_x$   
 313 reaction to produce nitrate ester compounds increasing with the size of the  $\text{RO}_2^\cdot$  molecule (Atkinson  
 314 et al., 1982). The  $\text{NO}_x$  concentrations in urban Beijing are approximately a factor of 10 higher than  
 315 seen at the Hyytiälä station in Finland as reported by Yan et al. (2016), and hence it is expected to  
 316 be a more significant peroxy radical terminator.

317

318 Despite the very large fluxes of anthropogenic organic pollutants in Beijing, biogenic emissions are  
 319 still an important source of reactive VOCs in the city, with abundant isoprene oxidation products  
 320 observed (see above), as well as monoterpene monomers ( $\text{C}_{10}\text{H}_{16}\text{O}_9$ ,  $\text{C}_{10}\text{H}_{15}\text{O}_9\text{N}$ ) and some dimer  
 321 products ( $\text{C}_{20}\text{H}_{30}\text{O}_{11}$ ,  $\text{C}_{20}\text{H}_{31}\text{O}_{11}\text{N}$ ). The time series of the signals of all  $\text{C}_5$ ,  $\text{C}_{10}$  and  $\text{C}_{20}$  molecules is  
 322 plotted in Figure 3b, with  $\text{C}_5$  species assumed to be isoprene dominated,  $\text{C}_{10}$  and  $\text{C}_{20}$  assumed to be  
 323 monoterpene dominated. Signals for isoprene oxidation products are higher, with abundant  
 324 isoprene nitrate and dinitrate products.  $\text{C}_{10}$  products show similar behaviour, with, for example,  
 325 several  $\text{C}_{10}\text{H}_{15}\text{O}_x\text{N}_x$   $x = 5-9$  compounds seen. The  $\text{C}_{20}$  signal intensities are low, and follow the  
 326 general formula  $\text{C}_{20}\text{H}_x\text{O}_y\text{N}_z$ , where  $x = 26-32$ ,  $y = 7-11$  and  $z = 0-2$ ; in Figure 3 the signal for  $\text{C}_{20}$   
 327 compounds has been multiplied by a factor of 50 for visibility. The low signals reflect the lack of  
 328  $\text{RO}_2^\cdot$  cross reactions necessary for the production of these accretion products.

329

330 Other identified peaks are plotted in Figure 3c. The  $\text{C}_2$ - $\text{C}_4$  components are summed together, these  
 331 being small organic acids such as malonic acid and oxalic acid, as well as products such as  
 332  $\text{C}_4\text{H}_7\text{O}_6\text{N}$ . Malonic acid is the most prominent here, seen both as an  $\text{NO}_3^-$  adduct ( $\text{C}_3\text{H}_4\text{O}_4\text{NO}_3^-$ ) and  
 333 a proton transfer product ( $\text{C}_3\text{H}_3\text{O}_4^-$ ) at a ratio of around 2:3. [Measurements of particle phase](#)

dicarboxylic acids in cities typically show greater concentrations of of oxalic acid than malonic (Ho et al., 2016), and these acids are primarily produced in the aqueous phase (Bikkina et al., 2014). Primary sources of dicarboxylic acid include fossil fuel combustion (Kawamura and Kaplan, 1987) and biomass burning (Narukawa et al., 1999), which are both plentiful in urban Beijing. The C<sub>6</sub>-C<sub>9</sub> components are assumed to be dominated by oxidation products of alkylbenzenes such as C<sub>8</sub>H<sub>12</sub>O<sub>5</sub>, although fragments of other compounds, i.e., monoterpenes, can also occupy this region (Isaacman-Vanwertz et al., 2018). It is assumed the majority of the signal for these peaks come from alkylbenzenes. This assumption is supported by the relative signal intensity ratios of the oxygen numbers of monomer C<sub>8</sub>H<sub>12</sub>O<sub>n</sub> compounds being similar to those seen for xylene oxidation products in previous work (Molteni et al., 2018). The largest fraction, C<sub>11</sub> through C<sub>18</sub>, includes the larger compounds, oxidation products of larger aromatics, or products of the cross reaction of smaller RO<sub>2</sub> radicals. Here they are grouped without more sophisticated disaggregation as they all follow much the same time series, species such as C<sub>11</sub>H<sub>11</sub>O<sub>8</sub>N following the same temporal trends as C<sub>15</sub>H<sub>16</sub>O<sub>9</sub> and C<sub>16</sub>H<sub>24</sub>O<sub>12</sub>.

Nearly all ions with the exception of the larger compounds attributed to the cross reaction of C<sub>10</sub> monomers follow similar temporal patterns, with the majority of peaks occurring in the daytime. This reflects the importance of the concentration of atmospheric oxidants. Some selected oxidation products are plotted against their precursor VOCs in Figure 4. The concentration of isoprene is plotted against the signal of a nitrate HOM product, C<sub>5</sub>H<sub>9</sub>NO<sub>6</sub> (Xiong et al., 2015; Lee et al., 2016), while monoterpenes are plotted against C<sub>10</sub>H<sub>16</sub>O<sub>9</sub> (Ehn et al., 2014; Berndt et al., 2016; Yan et al., 2016; Kirkby et al., 2016; Massoli et al., 2018), and C<sub>2</sub>-benzenes against C<sub>8</sub>H<sub>12</sub>O<sub>6</sub> (Molteni et al., 2018; Wang et al., 2017). The first half of the time series shows little correlation between the VOC species and the resultant oxidation products, while isoprene, monoterpenes and C<sub>2</sub>-benzenes follow their usual diurnal cycles, isoprene having the most distinct with a strong midday peak. The latter two days, however, show similar and coinciding peaks in both the VOCs and HOMs - HOMs show

afternoon peaks on both days, and an initial shelf on the final half day. The  $C_5H_9NO_6$  peak follows some of the peaks of the isoprene, but not all (e.g., morning shelf of isoprene on 24/06). Concentrations of isoprene do not seem to determine directly the signal of HOM, as the day with the lowest isoprene of all is the day with highest  $C_5H_9NO_6$ . The  $C_{10}H_{16}O_9$  trace has coincidental peaks with the monoterpene trace also, including two 4-hour separated simultaneous peaks on 25/06. The peaks in the concentrations of  $C_2$ -benzenes are nearly synchronous with the peaks in  $C_8H_{12}O_6$ , for which the data exhibit a strong mid afternoon peak likely due to the lack of an efficient ozonolysis reaction pathway; the main oxidant of  $C_2$ -benzenes is the  $OH^\cdot$  radical. Trends of both  $C_3$  benzenes and their HOMs are much the same as  $C_2$  benzenes as discussed above, pointing to similar sources and oxidation chemistries. . The concentration of precursor VOC is likely a driving force in the identity and quantity of various HOM products, but not the sole determinant, as while there are simultaneous peaks of VOCs and HOMs, both the condensation sink and oxidant concentrations also influence HOM product signals.

The first half of campaign measurements is marked by an episode of low HOM signals. A diurnal cycle still exists but it is weak. The radiation intensity was significantly lower on these prior days than it was on the 24th. No data is available for the final period of measurement. Ozone is higher on the prior measurement days with lower HOM signals (see Figure S1). Little agreement is seen between VOC concentration and HOM signals on these days. The condensational sinks are roughly similar to those on days of higher HOM concentrations, but temperature and solar radiation are much lower. HOM formation is largely dependent upon VOC concentration, oxidant concentration (which will be lower if solar radiation is lower, especially in the case of  $OH^\cdot$ , the main oxidant of aromatic species especially), and temperature (as H-shifts are highly temperature dependent) (Quéléver et al., 2019), as well as losses by  $RO_2^\cdot$  termination before a molecule can become HOM, and losses to condensational sink. The low HOM concentration is likely due to these lower temperatures, and weaker solar radiation not facilitating HOM formation.

386 ~~It is therefore plausible that light intensity, and therefore OH<sup>-</sup> concentration is one of the main~~  
387 ~~drivers of HOM concentrations in Beijing.~~

388

389 The C<sub>20</sub> compounds plotted in Figure 3b show no strong diurnal sequence, contrasting with other  
390 HOMs. We can presume that all C<sub>20</sub> compounds identified are the result of the reaction of two  
391 monoterpene C<sub>10</sub> RO<sub>2</sub><sup>•</sup> radicals, a reasonable assumption as all identified C<sub>20</sub> species follow the  
392 general formula outlined for these reactions (C<sub>20</sub>H<sub>28-32</sub>O<sub>6-16</sub>). The formation of C<sub>20</sub> dimers is  
393 dependent upon two processes, initial oxidation of monoterpenes, and RO<sub>2</sub>-RO<sub>2</sub> termination. Initial  
394 oxidation is contingent upon oxidant concentration, which is highest in the daytime, and RO<sub>2</sub>-RO<sub>2</sub><sup>•</sup>  
395 termination is contingent upon the probability of the molecular collision between the RO<sub>2</sub><sup>•</sup>  
396 molecules occurring before other radical termination (i.e., RO<sub>2</sub><sup>•</sup>-NO<sub>x</sub>, or RO<sub>2</sub><sup>•</sup>-HO<sub>2</sub><sup>•</sup>). There is likely  
397 a strong diurnal sequence in the dominant RO<sub>2</sub><sup>•</sup> termination mechanisms across the day period, and  
398 the combination of the two factors discussed above results in there being no strong diurnal trend in  
399 these molecules. A lower oxidant concentration at night results in less RO<sub>2</sub><sup>•</sup> molecules, but less NO  
400 and HO<sub>2</sub><sup>•</sup> results in a greater chance for those RO<sub>2</sub><sup>•</sup> molecules to dimerise (Rissanen, 2018, Garmash  
401 et al., 2019). As the levels of NO<sub>x</sub> in Beijing fall, the peroxy radical termination reactions will be  
402 less probable compared to continued autoxidation (Praske et al., 2018), and it is expected that more  
403 oxidised HOM products will be seen with lower volatilities and therefore a greater potential  
404 contribution to earlier stage particle formation and growth.

405

### 406 3.3. New Particle Formation

407 Nearly all the signal intensity in the CI-API-ToF instrument arises from molecules charged by NO<sub>3</sub><sup>-</sup>,  
408 therefore plotting the unit mass resolution data (the data gained by integrating over the entire area at  
409 each m/Q integer) against time describes simply the evolution of oxidised organic molecules, acids  
410 and their molecular clusters both with each other and stabilising amine species. This is done in  
411 Figure 5. As the signal intensity varies by factors of 10 from mass to mass, each value has been



normalised so they have maxima at 1. This has been done separately for two days for clarity, as the signal intensity also varies from day to day. PSM data for these two days is plotted in Figure 5 also, with both total particle count >1.30 nm in black and the number difference between the lower and upper size cuts (1.30 and 1.84 nm) in blue, which shows the number of particles between these sizes. The relationship between mass and electrical mobility diameter can be defined thus (Tammet, 1995),

$$d_e = \left(\frac{6m}{\pi\rho}\right)^{\frac{1}{3}} + d_g \quad (3)$$

where  $d_e$  is the electrical mobility diameter of the cluster or particle,  $m$  is the mass of the cluster or particle expressed in kg,  $\rho$  is the density and  $d_g$  is the effective gas diameter, determined to be 0.3 nm for smaller particles (Larriba et al., 2011). We can use this to draw a comparison between the PSM and CI-API-ToF measurements. If a density of 1.2 g cm<sup>-3</sup> is assumed, then once molecular clusters reach the >400  $m/Q$  range, they will be seen in the lowest size cut of the PSM, or >700  $m/Q$  if a density of 2.0 g cm<sup>-3</sup> is assumed. A full table of densities is provided in the Supplementary Information.

A burst in the signal seen by the CI-API-TOF occurs first in the late morning in the top panel of Figure 5, and this is at the same time as peaks begin to rise in the identified HOMs (see Figure 3). Here, the PSM is not available due to an instrumental fault until 16:00; however, at that point, an elevation to particle count and a large elevation to cluster count can be seen. Moving into the evening period, the mass contour shows peaks to larger masses >400  $m/Q$ . This is likely dimerised compounds and products of NO<sub>3</sub><sup>-</sup> chemistry with little contribution to newly forming particles, but still sensitive to chemical ionisation by NO<sub>3</sub><sup>-</sup>. Many of these peaks cannot be assigned due to uncertainties in the structural formula assignment for higher mass peaks, as the number of possible dimerised compounds is many, being the combination of most possible RO<sub>2</sub> radicals. Graphically,

437 these are over-represented in Figure 5 due to the normalisation, their signals (especially  $>500\ m/Q$ )  
438 are much lower than the signals  $<400\ m/Q$ .  
439  
440 The second day plotted in the lower panel of Figure 5 (25/06/2017) shows a strong afternoon peak  
441 to the HOMs (for most HOMs, stronger than that on the day prior). Particle formation is shown in  
442 the PSM data. A strong midday peak to particle number is seen with two distinct peaks to cluster  
443 count. These two peaks are not coincidental with the two peaks to HOM signal (i.e., nitrogen-  
444 containing HOMs in Figure 3a peaking at 11:00 and 16:00). Sulfuric acid, however, does peak  
445 synchronously with the particle number count. Sulfuric acid is plotted across the contour plot in  
446 Figure 6, where PSM data is also shown in the bottom panel. The peak to CI-APi-TOF mass signal,  
447 visible in Figure 5 occurs at around 12:00/13:00, peaks in the PSM cluster count occur at 10:00 and  
448 13:00. Peaks in mass up to  $550\ m/Q$  are seen in the CI-APi-ToF at 13:00. Assuming the density of  
449 these species is  $\leq 1.6\ g\ cm^{-3}$  then these will be suitably sized to be grown in the PSM saturator..  
450 These newly formed particles then go on to grow and contribute significantly to the larger particle  
451 count (Figure S3). As initial particle formation coincides with sulfuric acid signal peaks and before  
452 HOM signals peak, it can be assumed on these days, the HOM contribution to the initial particle  
453 formation is modest.  
454  
455 There is recent strong evidence to suggest that the driving force of the earliest stages of particle  
456 formation in urban Shanghai is from sulfuric acid and  $C_2$ -amines (Yao et al., 2018), and the  
457 coincidental peaks of sulfuric acid with new particles as seen in Figure 6 suggest a similar  
458 behaviour. Dimethylamine (DMA) can efficiently stabilise the sulfuric acid clusters (Almeida et al.,  
459 2013). Here, few larger sulfuric acid-DMA clusters were visible in the dataset, as seen in the work  
460 by Yao et al., 2018, although five sulfuric acid-dimethylamine (SA-DMA) ions were observed, the  
461 others were likely too low in signal to be confidently resolved from their neighbouring peaks;  
462 however, clusters of up to 4 sulfuric acid ~~ions~~ molecules and 3 dimethylamine molecules were seen,

with similar diurnal trends to sulfuric acid. The scarcity of SA-DMA clusters is likely due to instrumental conditions, rather than their absence in the atmosphere. The nitrate chemical ionisation system tends to evaporate amine compounds upon charging, and as specific voltage-tuning setups can lend themselves towards preservation or breakage of molecular clusters, the signal for larger sulfuric acid clusters was also very weak. The formation of HOM-sulfuric acid clusters is unlikely under atmospheric conditions (Elm et al., 2017) and few of these were observed. Signals of HOMs seem to coincide with later particle growth; it can be expected that HOM molecules make a more significant contribution to particle growth than to early particle formation, with the largest and most oxidised being involved in early growth, and the smaller and less oxidised contributing to later growth as the necessary vapour pressure properties become less demanding.

473

#### 4. CONCLUSIONS

The average degree of HOM oxidation in Beijing is comparable with that seen in other environments. Rapid intramolecular hydrogen shifts during autoxidation due to the higher temperatures are probably offset by the frequent termination reactions due to high  $\text{NO}_x$  concentrations.  $OS_c$  values seem to be marginally higher for biogenic species.

479

The temporal trend of nearly every HOM shows afternoon or evening maxima. Both  $\text{O}_3$  and  $\text{OH}\cdot$  have high daytime concentrations and these likely drive the initial oxidation steps. The species arising from alkylbenzene precursors show sharper afternoon peaks, probably since their oxidation is  $\text{OH}\cdot$  dominated. Many of the rest of the peaks, coming from largely BVOC precursors show broader daytime peaks, being influenced by  $\text{O}_3$  also. There seems to be no direct link between VOC concentrations and HOM signals, with days of lower precursor VOC sometimes having higher HOM signals and vice versa.

487

488 Initial particle formation coincides with peak sulfuric acid signals, while the growth of the particles  
489 correlates more closely with the signals of HOMs. This is very similar to behaviour observed in a  
490 study of NPF in Shanghai which was attributed to sulfuric acid-dimethylamine-water nucleation  
491 with condensing organic species contributing to particle growth (Yao et al., 2018), and this is  
492 further backed up by numerous SA-DMA clusters present in this dataset. The freshly formed  
493 particles grow and contribute significantly to total particle loading. This is visible when the unit  
494 mass CI-APi-ToF data is plotted as a contour plot, and further to this is visible in the PSM data,  
495 with bursts to both total number count >1.30 nm and the number of molecular clusters between 1.30  
496 and 1.84 nm. As NO<sub>x</sub> levels fall in Beijing due to traffic emission control measures being enforced  
497 it is likely that autoxidation will become increasingly significant in the new particle formation  
498 processes. The number of molecules detected by the NO<sub>3</sub> CIMS is undoubtedly many more than  
499 have had formulae assigned here, but to identify more requires a more sophisticated data  
500 deconvolution.

501

502

## 503 **DATA ACCESSIBILITY**

504 Data supporting this publication are openly available from the UBIRA eData repository at  
505 <https://doi.org/10.25500/edata.bham.00000304>

506

## 507 **AUTHOR CONTRIBUTIONS**

508 The study was conceived and planned by RMH and ZS. DCSB and JB set up and operated the  
509 main instrumental measurements, and JB prepared the first draft of the paper and responded to  
510 comments from RMH and ZS. CNH and WJA contributed the hydrocarbon data and provided  
511 comments on the draft manuscript, and ES and JL contributed the gas phase pollutant data.

512

## 513 **COMPETING INTERESTS**

514 The authors have no conflict of interests.

515

## 516 **ACKNOWLEDGMENTS**

517 This work was part of the APHH-Beijing programme funded by the UK Natural Environmentl  
518 Research Council (NE/N007190/1) and the Natural Sciences Funding Council of China. It was  
519 additionally facilitated by the National Centre for Atmospheric Science ODA national capability  
520 programme ACREW (NE/R000034/1), which is supported by NERC and the GCRF. We thank  
521 Professor X.M Wang from the Guangzhou Institute of Geochemistry, Chinese Academy of  
522 Sciences, Brian Davison from Lancaster University and Ben Langford, Eiko Nemitz, Neil  
523 Mullinger and other staff from the Centre for Ecology and Hydrology, Edinburgh for assistance  
524 with the VOC measurements and associated infrastructure.

525

## REFERENCES

- Alam, A., Shi, J.P., Harrison R.M.: Observations of new particle formation in urban air, *J. Geophys. Res.*, 108, 4093-4107, doi:10.1029/2001JD001417, 2003
- Almeida, J., Schobesberger, S., Kürten, A., Ortega, I. K., Kupiainen-Määttä, O., Praplan, A. P., Adamov, A., Amorim, A., Bianchi, F., Breitenlechner, M., David, A., Dommen, J., Donahue, N. M., Downard, A., Dunne, E., Duplissy, J., Ehrhart, S., Flagan, R. C., Franchin, A., Guida, R., Hakala, J., Hansel, A., Heinritzi, M., Henschel, H., Jokinen, T., Junninen, H., Kajos, M., Kangasluoma, J., Keskinen, H., Kupc, A., Kurtén, T., Kvashin, A. N., Laaksonen, A., Lehtipalo, K., Leiminger, M., Leppä, J., Loukonen, V., Makhmutov, V., Mathot, S., McGrath, M. J., Nieminen, T., Olenius, T., Onnela, A., Petäjä, T., Riccobono, F., Riipinen, I., Rissanen, M., Rondo, L., Ruuskanen, T., Santos, F. D., Sarnela, N., Schallhart, S., Schnitzhofer, R., Seinfeld, J. H., Simon, M., Sipilä, M., Stozhkov, Y., Stratmann, F., Tomé, A., Tröstl, J., Tsagkogeorgas, G., Vaattovaara, P., Viisanen, Y., Virtanen, A., Vrtala, A., Wagner, P. E., Weingartner, E., Wex, H., Williamson, C., Wimmer, D., Ye, P., Yli-Juuti, T., Carslaw, K. S., Kulmala, M., Curtius, J., Baltensperger, U., Worsnop, D. R., Vehkamäki, H., and Kirkby, J.: Molecular understanding of sulphuric acid-amine particle nucleation in the atmosphere, *Nature*, 502, 359-363, 2013.
- Atkinson, R., Aschmann, S. M., Carter, W. P. L., Winer, A. M., and Pitts, J. N.: Alkyl nitrate formation from the nitrogen oxide (NO<sub>x</sub>) air photooxidations of C2-C8 n-alkanes, *J. Phys. Chem.*, 86, 4563-4569, 1982.
- Berndt, T., Richters, S., Kaethner, R., Voigtländer, J., Stratmann, F., Sipilä, M., Kulmala, M., and Herrmann, H.: Gas-Phase Ozonolysis of Cycloalkenes: Formation of Highly Oxidized RO<sub>2</sub> Radicals and Their Reactions with NO, NO<sub>2</sub>, SO<sub>2</sub>, and Other RO<sub>2</sub> Radicals, *J. Phys. Chem. A.*, 119, 10336-10348, 2015.
- Berndt, T., Richters, S., Jokinen, T., Hyttinen, N., Kurtén, T., Otkjær, R. V., Kjaergaard, H. G., Stratmann, F., Herrmann, H., Sipilä, M., Kulmala, M., and Ehn, M.: Hydroxyl radical-induced formation of highly oxidized organic compounds, *Nature Comm.*, 7, 20 <https://doi.org/10.1038/ncomms13677>, 2016.
- Bianchi, F., Garmash, O., He, X., Yan, C., Iyer, S., Rosendahl, I., Xu, Z., Rissanen, M. P., Riva, M., Taipale, R., Sarnela, N., Petäjä, T., Worsnop, D. R., Kulmala, M., Ehn, M., and Junninen, H.: The role of highly oxygenated molecules (HOMs) in determining the composition of ambient ions in the boreal forest, *Atmos. Chem. Phys.*, 17, 13819-13831, 2017.
- Brook, R. D., Rajagopalan, S., Pope, C. A., Brook, J. R., Bhatnagar, A., Diez-Roux, A. V., Holguin, F., Hong, Y., Luepker, R. V., Mittleman, M. A., Peters, A., Siscovick, D., Smith, S. C., Whitsel, L., and Kaufman, J. D.: Particulate matter air pollution and cardiovascular disease: An update to the scientific statement from the american heart association, *Circulation*, 121, 2331-2378, 2010.
- Chu, B., Kerminen, V.-M., Bianchi, F., Yan, C., Petaja, T., and Kulmala, M.: Atmospheric new particle formation in China, *Atmos. Chem. Phys.*, 19, 115-138, 2019.
- Crounse, J. D., Nielsen, L. B., Jørgensen, S., Kjaergaard, H. G., and Wennberg, P. O.: Autoxidation of organic compounds in the atmosphere, *J. Phys. Chem. Lett.*, 4, 3513-3520, 2013.

577 Cubison, M. J. and Jimenez, J. L.: Statistical precision of the intensities retrieved from constrained  
578 fitting of overlapping peaks in high resolution mass spectra, *Atmos. Meas. Tech.*, 8, 2333-2345,  
579 2015.

580

581 Delfino, R. J., Sioutas, C., and Malik, S.: Potential role of ultrafine particles in associations between  
582 airborne particle mass and cardiovascular health, *Environ. Health Perspect.*, 113, 934-946, 2005.

583

584 Ehn, M., Thornton, J. A., Kleist, E., Sipilä, M., Junninen, H., Pullinen, I., Springer, M., Rubach, F.,  
585 Tillmann, R., Lee, B., Lopez-Hilfiker, F., Andres, S., Acir, I.-H., Rissanen, M., Jokinen, T.,  
586 Schobesberger, S., Kangasluoma, J., Kontkanen, J., Nieminen, T., Kurtén, T., Nielsen,  
587 L. B., Jørgensen, S., Kjaergaard, H. G., Canagaratna, M., Maso, M. D., Berndt, T., Petäjä, T.,  
588 Wahner, A., Kerminen, V.-M., Kulmala, M., Worsnop, D. R., Wildt, J., and Mentel, T. F.: A large  
589 source of low-volatility secondary organic aerosol, *Nature*, 506, 476-479, 2014.

590

591 Elm, J., Myllys, N., and Kurtén, T.: What is Required for Highly Oxidized Molecules to Form  
592 Clusters with Sulfuric Acid?, *J. Phys. Chem. A*, 121, 4578-4587, 2017.

593

594 Garmash, O., Rissanen, M. P., Pullinen, I., Schmitt, S., Kausiala, O., Tillmann, R., Percival, C.,  
595 Bannan, T. J., Priestley, M., Hallquist, Å. M., Kleist, E., Kiendler-Scharr, A., Hallquist, M., Berndt,  
596 T., McFiggans, G., Wildt, J., Mentel, T., and Ehn, M.: Multi-generation OH oxidation as a source  
597 for highly oxygenated organic molecules from aromatics, *Atmos. Chem. Phys. Discuss.*,  
598 <https://doi.org/10.5194/acp-2019-582>, in review, 2019.

599

600 Gong, Y., Hu, M., Cheng, Y., Su, H., Yue, D., Liu, F., Wiedensohler, A., Wang, Z., Kalesse, H.,  
601 Liu, S., Wu, Z., Xiao, K., Mi, P., and Zhang, Y.: Competition of coagulation sink and source rate:  
602 New particle formation in the Pearl River Delta of China, *Atmos. Environ.*, 44, 3278-3285, 2010.

603

604 Guo, S., Hu, M., Zamora, M. L., Peng, J., Shang, D., Zheng, J., Du, Z., Wu, Z., Shao, M., Zeng, L.,  
605 Molina, M. J., and Zhang, R.: Elucidating severe urban haze formation in China., *PNAS*, 111,  
606 17373- 17378, 2014.

607

608 [Ho, K. F., Lee, S. C., Ho, S. S. H., Kawamura, K., Tachibana, E., Cheng, Y. and Zhu, T.: Dicarboxylic  
609 acids, ketocarboxylic acids,  \$\alpha\$ -dicarbonyls, fatty acids, and benzoic acid in urban aerosols collected  
610 during the 2006 Campaign of Air Quality Research in Beijing \(CAREBeijing-2006\), \*J. Geophys. Res.\*  
611 \*Atmos.\*, 115\(19\), 1–14, doi:10.1029/2009JD013304, 2010.](#)

612

613 Hyttinen, N., Kupiainen-Määttä, O., Rissanen, M. P., Muuronen, M., Ehn, M., and Kurtén, T.:  
614 Modeling the Charging of Highly Oxidized Cyclohexene Ozonolysis Products Using Nitrate-Based  
615 Chemical Ionization, *J. Phys. Chem., A*, 119, 6339-6345, 2015.

616

617 Isaacman-Vanwertz, G., Massoli, P., O'Brien, R., Lim, C., Franklin, J. P., Moss, J. A., Hunter, J. F.,  
618 Nowak, J. B., Canagaratna, M. R., Misztal, P. K., Arata, C., Roscioli, J. R., Herndon, S. T., Onasch,  
619 T. B., Lambe, A. T., Jayne, J. T., Su, L., Knopf, D. A., Goldstein, A. H., Worsnop, D. R., and Kroll,  
620 J. H.: Chemical evolution of atmospheric organic carbon over multiple generations of oxidation,  
621 *Nature Chem.*, 10, 462-468, <https://doi.org/10.1038/s41557-018-0002-2>, 2018

622

623 Jokinen, T., Sipilä, M., Junninen, H., Ehn, M., Lönn, G., Hakala, J., Petäjä, T., Mauldin, R. L.,  
624 Kulmala, M., and Worsnop, D. R.: Atmospheric sulphuric acid and neutral cluster measurements  
625 using CI-API-TOF, *Atmos. Chem. Phys.*, 12, 4117-4125, 2012.

626

627 Jokinen, T., Sipilä, M., Richters, S., Kerminen, V. M., Paasonen, P., Stratmann, F., Worsnop, D.,  
628 Kulmala, M., Ehn, M., Herrmann, H., and Berndt, T.: Rapid autoxidation forms highly oxidized

RO2 radicals in the atmosphere, *Angewandte Chemie - International Edition*, 53, 14596-14600, <https://doi.org/10.1002/anie.201408566>, 2014.

Junninen, H., Ehn, M., Petäjä, Luosujärvi, L., Kotiaho, T., Kostiainen, R., Rohner, U., Gonin, M., Fuhrer, K., Kulmala, M., and Worsnop, D. R.: A high-resolution mass spectrometer to measure atmospheric ion composition, *Atmos. Meas. Tech.*, 3, 1039-1053, 2010.

Kerminen, V. M., Paramonov, M., Anttila, T., Riipinen, I., Fountoukis, C., Korhonen, H., Asmi, E., Laakso, L., Lihavainen, H., Swietlicki, E., Svenningsson, B., Asmi, A., Pandis, S. N., Kulmala, M., and Petäjä, T.: Cloud condensation nuclei production associated with atmospheric nucleation: A synthesis based on existing literature and new results, *Atmos. Chem. Phys.*, 12, 12037-12059, 2012.

[Kawamura, K. and Kaplan, I. R.: Motor Exhaust Emissions as a Primary Source for Dicarboxylic Acids in Los Angeles Ambient Air, \*Environ. Sci. Technol.\*, 21\(1\), 105–110, doi:10.1021/es00155a014, 1987.](#)

Khan, M., Cooke M, Utembe, S., Archibald A., Derwent, R., Jenkin, M., Morris, W., South, N., Hansen, J., Francisco, J., Percival, C., Shallcross, D.: Global analysis of peroxy radicals and peroxy radical-water complexation using the STOCHEM-CRI global chemistry and transport model, *Atmos. Environ.*, 106, 278-287, 2015.

Kirkby, J., Curtius, J., Almeida, J., Dunne, E., Duplissy, J., Ehrhart, S., Franchin, A., Gagné, S., Ickes, L., Kürten, A., Kupc, A., Metzger, A., Riccobono, F., Rondo, L., Schobesberger, S., Tsagkogeorgas, G., Wimmer, D., Amorim, A., Bianchi, F., Breitenlechner, M., David, A., Dommen, J., Downard, A., Ehn, M., Flagan, R. C., Haider, S., Hansel, A., Hauser, D., Jud, W., Junninen, H., Kreissl, F., Kvashin, A., Laaksonen, A., Lehtipalo, K., Lima, J., Lovejoy, E. R., Makhmutov, V., Mathot, S., Mikkilä, J., Minginette, P., Mogo, S., Nieminen, T., Onnela, A., Pereira, P., Petäjä, T., Schnitzhofer, R., Seinfeld, J. H., Sipilä, M., Stozhkov, Y., Stratmann, F., Tomé, A., Vanhanen, J., Viisanen, Y., Vrtala, A., Wagner, P. E., Walther, H., Weingartner, E., Wex, H., Winkler, P. M., Carslaw, K. S., Worsnop, D. R., Baltensperger, U., and Kulmala, M.: Role of sulphuric acid, ammonia and galactic cosmic rays in atmospheric aerosol nucleation, *Nature*, 476, 429-435, <https://doi.org/10.1038/nature10343>, 2011.

Kirkby, J., Duplissy, J., Sengupta, K., Frege, C., Gordon, H., Williamson, C., Heinritzi, M., Simon, M., Yan, C., Almeida, J., Trostl, J., Nieminen, T., Ortega, I. K., Wagner, R., Adamov, A., Amorim, A., Bernhammer, A. K., Bianchi, F., Breitenlechner, M., Brilke, S., Chen, X., Craven, J., Dias, A., Ehrhart, S., Flagan, R. C., Franchin, A., Fuchs, C., Guida, R., Hakala, J., Hoyle, C. R., Jokinen, T., Junninen, H., Kangasluoma, J., Kim, J., Krapf, M., Kurten, A., Laaksonen, A., Lehtipalo, K., Makhmutov, V., Mathot, S., Molteni, U., Onnela, A., Perakyla, O., Piel, F., Petaja, T., Praplan, A. P., Pringle, K., Rap, A., Richards, N. A., Riipinen, I., Rissanen, M. P., Rondo, L., Sarnela, N., Schobesberger, S., Scott, C. E., Seinfeld, J. H., Sipilä, M., Steiner, G., Stozhkov, Y., Stratmann, F., Tomé, A., Virtanen, A., Vogel, A. L., Wagner, A. C., Wagner, P. E., Weingartner, E., Wimmer, D., Winkler, P. M., Ye, P., Zhang, X., Hansel, A., Dommen, J., Donahue, N. M., Worsnop, D. R., Baltensperger, U., Kulmala, M., Carslaw, K. S., and Curtius, J.: Ion-induced nucleation of pure biogenic particles, *Nature*, 533, 521-526, <https://doi.org/10.1038/nature17953>, 2016.

Kroll, J. H., Donahue, N. M., Jimenez, J. L., Kessler, S. H., Canagaratna, M. R., Wilson, K. R., Altieri, K. E., Mazzoleni, L. R., Wozniak, A. S., Bluhm, H., Mysak, E. R., Smith, J. D., Kolb, C. E., and Worsnop, D. R.: Carbon oxidation state as a metric for describing the chemistry of atmospheric organic aerosol, *Nature Chemistry*, 3, 133-139, <https://doi.org/10.1038/nchem.948>, 2011.



681 Kulmala, M., Petäjä, T., Mönkkönen, P., Koponen, I. K., Dal Maso, M., Aalto, P. P., Lehtinen, K.  
682 E. J., and Kerminen, V.-M.: On the growth of nucleation mode particles: source rates of  
683 condensable vapor in polluted and clean environments, *Atmos. Chem. Phys.*, 5, 409-416, 2005.  
684

685 Kulmala, M., Petäjä, T., Nieminen, T., Sipilä, M., Manninen, H. E., Lehtipalo, K., Dal Maso, M.,  
686 Aalto, P. P., Junninen, H., Paasonen, P., Riipinen, I., Lehtinen, K. E. J., Laaksonen, A., and  
687 Kerminen, V.-M.: Measurement of the nucleation of atmospheric aerosol particles, *Nature*  
688 *Protocols*, 7, 1651-1667, <https://doi.org/10.1038/nprot.2012.091>, 2012.  
689 Kürten, A., Rondo, L., Ehrhart, S., and Curtius, J.: Calibration of a chemical ionization mass  
690 spectrometer for the measurement of gaseous sulfuric acid, *J. Phys. Chem., A*, 116, 6375-6386.  
691

692 Kurtén, T., Rissanen, M. P., Mackeprang, K., Thornton, J. A., Hyttinen, N., Jørgensen, S., Ehn, M.,  
693 and Kjaergaard, H. G.: Computational Study of Hydrogen Shifts and Ring-Opening Mechanisms in  
694  $\alpha$ -Pinene Ozonolysis Products, *J. Phys. Chem., A*, 119, 11366-11375, 2015.  
695

696 Kurtén, T., Tiusanen, K., Roldin, P., Rissanen, M., Luy, J. N., Boy, M., Ehn, M., and Donahue, N.:  
697  $\alpha$ -Pinene autoxidation products may not have extremely low saturation vapor pressures despite high  
698 O:C ratios, *J. Phys. Chem., A*, 120, 2569-2582, 2016.  
699

700 Larriba, C., Hogan, C. J., Attoui, M., Borrajo, R., Garcia, J. F., and De La Mora, J. F.: The  
701 mobility-volume relationship below 3.0 nm examined by tandem mobility-mass measurement,  
702 *Aerosol Sci. Techn.*, 45, 453-467, 2011.  
703

704 Lee, B. H., Mohr, C., Lopez-Hilfiker, F. D., Lutz, A., Hallquist, M., Lee, L., Romer, P., Cohen, R.  
705 C., Iyer, S., Kurtén, T., Hu, W., Day, D. A., Campuzano-Jost, P., Jimenez, J. L., Xu, L., Ng, N. L.,  
706 Guo, H., Weber, R. J., Wild, R. J., Brown, S. S., Koss, A., de Gouw, J., Olson, K., Goldstein, A. H.,  
707 Seco, R., Kim, S., McAvey, K., Shepson, P. B., Starn, T., Baumann, K., Edgerton, E. S., Liu, J.,  
708 Shilling, J. E., Miller, D. O., Brune, W., Schobesberger, S., D'Ambro, E. L., and Thornton, J. A.:  
709 Highly functionalized organic nitrates in the southeast United States: Contribution to secondary  
710 organic aerosol and reactive nitrogen budgets, *PNAS*, 113, 1516-1521, 2016.  
711

712 Lehtipalo, K., Yan, C., Dada, L., Bianchi, F., Xiao, M., Wagner, R., Stolzenburg, D., Ahonen, L. R.,  
713 Amorim, A., Baccarini, A., Bauer, P. S., Baumgartner, B., Bergen, A., Bernhammer, A.,  
714 K., Breitenlechner, M., Brilke, S., Buchholz, A., Mazon, S. B., Chen, D., Chen, X., Dias, A.,  
715 Dommen, J., Draper, D. C., Duplissy, J., Ehn, M., Finkenzeller, H., Fischer, L., Frege, C., Fuchs,  
716 C., Garmash, O., Gordon, H., Hakala, J., He, X., Heikkinen, L., Heinritzi, M., Helm, J. C., Hofbauer,  
717 V., Hoyle, C. R., Joki-nen, T., Kangasluoma, J., Kerminen, V.-M., Kim, C., Kirkby, J., Kontkanen,  
718 J., Kürten, A., Lawler, M. J., Mai, H., Mathot, S., Mauldin, R. L., Molteni, U., Nichman, L., Nie,  
719 W., Niemi-nen, T., Ojdanic, A., Onnela, A., Passananti, M., Petäjä, T., Piel, S. F., Pospisilova, V.,  
720 Quéléver, L. L. J., Rissanen, M. P., Rose, C., Sarnela, N., Schallhart, S., Schuchmann, S., Sengupta,  
721 K., Simon, M., Sipilä, M., Tauber, C., Tomé, A., Tröstl, J., Väisä-nen, O., Vogel, A. L., Volkamer,  
722 R., Wagner, A. C., Wang, M., Weitz, L., Wimmer, D., Ye, P., Ylisirniö, A., Zha, Q., Carslaw, K. S.,  
723 Curtius, J., Donahue, N. M., Flagan, R. C., Hansel, A., Riipinen, I., Virtanen, A., Winkler, P. M.,  
724 Baltensperger, U., Kulmala, M., and Worsnop, D. R.: Multicomponent new particle formation from  
725 sulfuric acid, ammonia, and biogenic vapors, *Science Advances*, 4,  
726 <https://doi.org/10.1126/sciadv.aau5363>, 2018.  
727

728 Massoli, P., Stark, H., Canagaratna, M. R., Krechmer, J. E., Xu, L., Ng, N. L., Mauldin, R. L., Yan,  
729 C., Kimmel, J., Miszta, P. K., Jimenez, J. L., Jayne, J. T., and Worsnop, D. R.: Ambient  
730 Measurements of Highly Oxidized Gas-Phase Molecules during the Southern Oxidant and Aerosol  
731 Study (SOAS) 2013, *ACS Earth Space Chem.*, 2, 653-672, 2018.  
732

733 McMurry, P. H., Shan Woo, K., Weber, R., Chen, D.-R., and Pui, D. Y. H.: Size distributions of 3-  
734 10 nm atmospheric particles: implications for nucleation mechanisms, *Philosophical Transactions*  
735 *of the Royal Society A: Math., Phys. Eng. Sci.*, 358, 2625-2642, 2000.

736

737 Miller, M. R., Raftis, J. B., Langrish, J. P., McLean, S. G., Samutrtai, P., Connell, S. P., Wilson, S.,  
738 Vesey, A. T., Fokkens, P. H., Boere, A. J. F., Krystek, P., Campbell, C. J., Hadoke, P. W.,  
739 Donaldson, K., Cassee, F. R., Newby, D. E., Duffin, R., and Mills, N. L.: Inhaled nanoparticles  
740 accumulate at sites of vascular disease, *ACS Nano*, 11, 4542-4552, 2017.

741 Møller, K. H., Tram, C. M., and Kjaergaard, H. G.: Side-by-Side Comparison of Hydroperoxide  
742 and Corresponding Alcohol as HydrogenBond Donors, *J. Phys. Chem. A*, 121, 2951-2959, 2017.

743

744 Molteni, U., Bianchi, F., Klein, F., Haddad, I. E., Frege, C., Rossi, M. J., Dommen, J., and  
745 Baltensperger, U.: Formation of highly oxygenated organic molecules from aromatic compounds,  
746 *Atmos. Chem. Phys.*, 18, 1909-1921, 2018.

747

748 Mutzel, A., Poulain, L., Berndt, T., Iinuma, Y., Rodigast, M., Böge, O., Richters, S., Spindler, G.,  
749 Sipila, M., Jokinen, T., Kulmala, M., Herrmann, H.: Highly oxidized multifunctional organic  
750 compounds observed in tropospheric particles: A field and laboratory study, *Environ. Sci. Technol.*,  
751 49, 7754-7761, 2015.

752

753 Myllys, N., Olenius, T., Kurtén, T., Vehkamäki, H., Riipinen, I., and Elm, J.: Effect of Bisulfate,  
754 Ammonia, and Ammonium on the Clustering of Organic Acids and Sulfuric Acid, *J. Phys. Chem.*  
755 *A*, 121, 4812-4824, 2017.

756

757 [Narukawa, M., Kawamura, K., Takeuchi, N. and Nakajima, T.: Distribution of dicarboxylic acids](#)  
758 [and carbon isotopic ratios in aerosols from 1997 Indonesian forest fires, \*Geophys. Res. Lett.\*,](#)  
759 [26\(10\), 3101–3104, 1999.](#)

760

761 Penner, J. E., Xu, L., and Wang, M.: Satellite methods underestimate indirect climate forcing by  
762 aerosols., *PNAS*, 108, 13404-13408, 2011.

763

764 Praske, E., Otkjær, R. V., Crounse, J. D., Hethcox, J. C., Stoltz, B. M., Kjaergaard, H. G., and  
765 Wennberg, P. O.: Atmospheric autoxidation is increasingly important in urban and suburban North  
766 America, *PNAS*, 115, 64-69, 2018.

767

768 Qi, X., Ding, A., Roldin, P., Xu, Z., Zhou, P., Sarnela, N., Nie, W., Huang, X., Rusanen, A., Ehn,  
769 M., Rissanen, M. P., Petäjä, T., Kulmala, M., and Boy, M.: Modelling studies of HOMs and their  
770 contributions to new particle formation and growth: comparison of boreal forest in Finland and a  
771 polluted environment in China, *Atmos. Chem. Phys.*, 18, 11779-11791, 2018.

772

773 [Quéléver, L. L. J., Kristensen, K., Normann Jensen, L., Rosati, B., Teiwes, R., Daellenbach, K. R.,](#)  
774 [Peräkylä, O., Roldin, P., Bossi, R., Pedersen, H. B., Glasius, M., Bilde, M., and Ehn, M.: Effect of](#)  
775 [temperature on the formation of highly oxygenated organic molecules \(HOMs\) from alpha-pinene](#)  
776 [ozonolysis, \*Atmos. Chem. Phys.\*, 19, 7609–7625, <https://doi.org/10.5194/acp-19-7609-2019>, 2019.](#)

777

778 ~~[Quéléver, J., Kristensen, K., Normann Jensen, L., Teiwes, R., Daellenbach, Kaspar R., Peräkylä,](#)~~  
779 ~~[O., Roldin, P., Pedersen, H., Glasius, M., Bilde, M., Ehn, M.: Effect of temperature on the](#)~~  
780 ~~[formation of Highly-oxygenated Organic Molecules \(HOM\) from alpha-pinene ozonolysis, \*Atmos.\*](#)~~  
781 ~~[Chem. Phys. Discuss.](#), 18, 1–29, 2018.~~

782

783 Riccobono, F., Schobesberger, S., Scott, C., Dommen, J., Ortega, I., Rondo, L., Almeida, J.,  
784 Amorim, A., Bianchi, F., Breitenlechner, M., David, A., Downard, A., Dunne, E., Duplissy, J.,

785 Ehrhart, S., Flagan, R., Franchin, A., Hansel, A., Junninen, H., Kajos, M., Keskinen, H., Kupc, A.,  
786 Kürten, A., Kvashin, A., Laaksonen, A., Lehtipalo, K., Makhmutov, V., Mathot, S., Nieminen, T.,  
787 Onnela, A., Petäjä, T., Praplan, A., Santos, F., Schallhart, S., Seinfeld, J., Sipilä, M., Van Spracklen,  
788 D., Stozhkov, Y., Stratmann, F., Tomé, A., Tsagkogeorgas, G., Vaattovaara, P., Viisanen, Y.,  
789 Vrtala, A., Wagner, P., Weingartner, E., Wex, H., Wimmer, D., Carslaw, K., Curtius, J., Donahue,  
790 N., Kirkby, J., Kulmala, M., Worsnop, D., and Baltensperger, U.: Oxidation products of biogenic  
791 emissions contribute to nucleation of atmospheric particles, *Science*, 344, 717-721, 2014.  
792  
793 Rissanen, M. P., Kurtén, T., Sipilä, M., Thornton, J. A., Kangasluoma, J., Sarnela, N., Junninen, H.,  
794 Jørgensen, S., Schallhart, S., Kajos, M. K., Taipale, R., Springer, M., Mentel, T. F., Ruuskanen, T.,  
795 Petäjä, T., Worsnop, D. R., Kjaergaard, H. G., and Ehn, M.: The formation of highly oxidized  
796 multifunctional products in the ozonolysis of cyclohexene, *J. Am. Chem. Soc.*, 136, 15596-15606  
797 2014.  
798  
799 Rissanen, M. P.: NO<sub>2</sub> Suppression of Autoxidation–Inhibition of Gas-Phase Highly Oxidized Dimer  
800 Product Formation, *ACS Earth Space Chem.*, 2, 1211–1219,  
801 <https://doi.org/10.1021/acsearthspacechem.8b00123>, 2018.  
802 Rose, C., Zha, Q., Dada, L., Yan, C., Lehtipalo, K., Junninen, H., Mazon, S. B., Jokinen, T.,  
803 Sarnela, N., Sipilä, M., Petäjä, T., Kerminen, V.-M., Bianchi, F., and Kulmala, M.: Observations of  
804 biogenic ion-induced cluster formation in the atmosphere, *Sci. Adv.*, 4, eaar5218,  
805 <https://doi.org/10.1126/sciadv.aar5218>, 2018.  
806  
807 Schobesberger, S., Junninen, H., Bianchi, F., Lönn, G., Ehn, M., Lehtipalo, K., Dommen, J.,  
808 Ehrhart, S., Ortega, I. K., Franchin, A., Nieminen, T., Riccobono, F., Hutterli, M., Duplissy, J.,  
809 Almeida, J., Amorim, A., Breitenlechner, M., Downard, A. J., Dunne, E. M., Flagan, R. C., Kajos,  
810 M., Keskinen, H., Kirkby, J., Kupc, A., Kürten, A., Kurtén, T., Laaksonen, A., Mathot, S., Onnela,  
811 A., Praplan, A. P., Rondo, L., Santos, F. D., Schallhart, S., Schnitzhofer, R., Sipilä, M., Tomé, A.,  
812 Tsagkogeorgas, G., Vehkamäki, H., Wimmer, D., Baltensperger, U., Carslaw, K. S., Curtius, J.,  
813 Hansel, A., Petäjä, T., Kulmala, M., Donahue, N. M., and Worsnop, D. R.: Molecular  
814 understanding of atmospheric particle formation from sulfuric acid and large oxidized organic  
815 molecules., *PNAS*, 110, 17223-17228, 2013.  
816  
817 Shi, J. P., Evans, D. E., Khan, A. A., and Harrison, R. M.: Sources and concentration of  
818 nanoparticles (<10nm diameter) in the urban atmosphere, *Atmos. Environ.*, 35, 1193-1202, 2001.  
819  
820 Shi, Z., Vu, T., Kotthaus, S., Harrison, R.M., Grimmond, S., Yue, S., Zhu, T., Lee, J., Han, Y.,  
821 Demuzere, M., Dunmore, R.E., Ren, L., Liu, D., Wang, Y., Wild, O., Allan, J., Acton, W.J.,  
822 Barlow, J., Barratt, B., Beddows, D., Bloss, W.J., Calzolari, G., Carruthers, D., Carslaw, D.C., Chan,  
823 Q., Chatzidiakou, L., Chen, Y., Crilley, L., Coe, H., Dai, T., Doherty, R., Duan, F., Fu, P., Ge, B.,  
824 Ge, M., Guan, D., Hamilton, J.F., He, K., Heal, M., Heard, D., Hewitt, C.N., Hollaway, M., Hu, M.,  
825 Ji, X. Jiang, R. Jones, M. Kalberer, F.J. Kelly, L. Kramer, B. Langford, C. Lin, A.C. Lewis, J. Li,  
826 W. Li, D., Liu, H., Liu, J., Loh, M., Lu, K., Lucarelli, F., Mann, G., McFiggans, G., Miller, M.R.,  
827 Mills, G., Monk, P., Nemitz, E., O'Connor, F., Ouyang, B., Palmer, P.I., Percival, C., Popoola, O.,  
828 Reeves, C., Rickard, A.R., Shao, L., Shi, G., Spracklen, D., Stevenson, D., Sun, Y., Sun, Z., Tao, S.,  
829 Tong, S., Wang, Q., Wang, W., Wang, X., Wang, X., Wang, Z., Wei, L., Whalley, L., Wu, X., Wu,  
830 Z., Xie, P., Yang, F., Zhang, Q., Zhang, Y., Zhang, Y. and Zheng, M.: In-depth study of air  
831 pollution sources and processes within Beijing and its surrounding region (APHH-Beijing), *Atmos.*  
832 *Chem. Phys.*, 19, 7519-7546, 2019.  
833  
834 Stolzenburg, D., Fischer, L., Vogel, A., Heinritzi, M., Schervish, M., Simon, M., Wagner, A.,  
835 Dada, L., Ahonen, L., Amorim, A., Baccarini, A., Bauer, P., Baumgartner, B., Bergen, A.,  
836 Bianchi, F., Breitenlechner, M., Brilke, S., Buenrostro Mazon, S., Chen, D., Dias, A., Draper, D.,

837 Duplissy, J., El Haddad, I., Finkenzeller, H., Frege, C., Fuchs, C., Garmash, O., Gordon, H., He, X.,  
838 Helm, J., Hofbauer, V., Hoyle, C., Kim, C., Kirkby, J., Kontkanen, J., Kürten, A., Lampilahti, J.,  
839 Lawler, M., Lehtipalo, K., Leiminger, M., Mai, H., Mathot, S., Mentler, B., Molteni, U., Nie, W.,  
840 Nieminen, T., Nowak, J., Ojdanic, A., Onnela, A., Passananti, M., Petäjä, T., Quéléver, L.,  
841 Rissanen, M., Sarnela, N., Schallhart, S., Tauber, C., Tomé, A., Wagner, R., Wang, M., Weitz, L.,  
842 Wimmer, D., Xiao, M., Yan, C., Ye, P., Zha, Q., Baltensperger, U., Curtius, J., Dommen, J., Flagan,  
843 R., Kulmala, M., Smith, J., Worsnop, D., Hansel, A., Donahue, N., Winkler, P., Rapid growth of  
844 organic aerosol nanoparticles over a wide tropospheric temperature range, *PNAS*, 115, 9122-9127,  
845 2018.

846

847 Tammet, H.: Size and mobility of nanometer particles, clusters and ions, *J. Aerosol Sci.*, 26, 459-  
848 475, 1995.

849

850 Tomasi, C., Fuzzi, S., Kokhanovsky, A.: *Atmospheric Aerosols: Life Cycles and Effects on Air*  
851 *Quality and Climate*, Wiley, 2016.

852

853 Tröstl, J., Chuang, W. K., Gordon, H., Heinritzi, M., Yan, C., Molteni, U., Ahlm, L., Frege, C.,  
854 Bianchi, F., Wagner, R., Simon, M., Lehtipalo, K., Williamson, C., Craven, J. S., Duplissy, J.,  
855 Adamov, A., Almeida, J., Bernhammer, A. K., Breitenlechner, M., Brilke, S., Dias, A., Ehrhart, S.,  
856 Flagan, R. C., Franchin, A., Fuchs, C., Guida, R., Gysel, M., Hansel, A., Hoyle, C. R., Jokinen, T.,  
857 Junninen, H., Kangasluoma, J., Keskinen, H., Kim, J., Krapf, M., Kürten, A., Laaksonen, A.,  
858 Lawler, M., Leiminger, M., Mathot, S., Möhler, O., Nieminen, T., Onnela, A., Petäjä, T., Piel, F.  
859 M., Miettinen, P., Rissanen, M. P., Rondo, L., Sarnela, N., Schobesberger, S., Sengupta, K., Sipilä,  
860 M., Smith, J. N., Steiner, G., Tomé, A., Virtanen, A., Wagner, A. C., Weingartner, E., Wimmer, D.,  
861 Winkler, P. M., Ye, P., Carslaw, K. S., Curtius, J., Dommen, J., Kirkby, J., Kulmala, M., Riipinen,  
862 I., Worsnop, D. R., Donahue, N. M., and Baltensperger, U.: The role of low-volatility organic  
863 compounds in initial particle growth in the atmosphere, *Nature*, 533, 527-531,  
864 <https://doi.org/10.1038/nature18271>, 2016.

865

866 Wang, S., Wu, R., Berndt, T., Ehn, M., and Wang, L.: Formation of Highly Oxidized Radicals and  
867 Multifunctional Products from the Atmospheric Oxidation of Alkylbenzenes, *Environ. Sci. Techn.*,  
868 51, 8442-8449, 2017.

869

870 Wang, Z., Wu, Z., Yue, D., Shang, D., Guo, S., Sun, J., Ding, A., Wang, L., Jiang, J., Guo, H., Gao,  
871 J., Cheung, H. C., Morawska, L., Keywood, M., and Hu, M.: New particle formation in China:  
872 Current knowledge and further directions, *Sci. Tot. Environ.*, 577, 258-266, 2016.

873

874 Wiedensohler, A., Cheng, Y. F., Nowak, A., Wehner, B., Achtert, P., Berghof, M., Birmili, W., Wu,  
875 Z. J., Hu, M., Zhu, T., Takegawa, N., Kita, K., Kondo, Y., Lou, S. R., Hofeumahauss, A., Holland,  
876 F., Wahner, A., Gunthe, S. S., Rose, D., Su, H., and Pöschl, U.: Rapid aerosol particle growth and  
877 increase of cloud condensation nucleus activity by secondary aerosol formation and condensation:  
878 A case study for regional air pollution in northeastern China, *Journal of Geophysical Research*  
879 *Atmospheres*, 114, 1–13, <https://doi.org/10.1029/2008JD010884>, 2009.

880

881 Wu, Z., Hu, M., Lin, P., Liu, S., Wehner, B., and Wiedensohler, A.: Particle number size  
882 distribution in the urban atmosphere of Beijing, China, *Atmos. Environ.*, 42, 7967-7980, 2008.

883

884 Wu, Z., Ma, N., Größ, J., Kecorius, S., Lu, K., Shang, D., Wang, Y., Wu, Y., Zeng, L., Hu, M.,  
885 Wiedensohler, A., and Zhang, Y.: Thermodynamic properties of nanoparticles during new particle  
886 formation events in the atmosphere of North China Plain, *Atmos. Res.*, 188, 55-63, 2017.

887

888 Wu, Z. J., Hu, M., Liu, S., Wehner, B., Bauer, S., Ssling, a. M., Wiedensohler, a., Petäjä, T., Dal

889 Maso, M., and Kulmala, M.: New particle formation in Beijing, China: Statistical analysis of a 1-  
890 year data set, *J. Geophys. Res. Atmospheres*, 112, D09209, <https://doi.org/10.1029/2006JD007406>,  
891 2007.

892

893 Xiong, F., McAvey, K. M., Pratt, K. A., Groff, C. J., Hostetler, M. A., Lipton, M. A., Starn, T. K.,  
894 Seeley, J. V., Bertman, S. B., Teng, A. P., Crounse, J. D., Nguyen, T. B., Wennberg, P. O., Misztal,  
895 P. K., Goldstein, A. H., Guenther, A. B., Koss, A. R., Olson, K. F., De Gouw, J. A., Baumann, K.,  
896 Edgerton, E. S., Feiner, P. A., Zhang, L., Miller, D. O., Brune, W. H., and Shepson, P. B.:  
897 Observation of isoprene hydroxynitrates in the Southeastern United States and implications for the  
898 fate of NO<sub>x</sub>, *Atmos. Chem. Phys.*, 15, 11257-11272, 2015 .

899

900 Yan, C., Nie, W., Äijälä, M., Rissanen, M. P., Canagaratna, M. R., Massoli, P., Junninen, H.,  
901 Jokinen, T., Sarnela, N., Häme, S. A. K., Schobesberger, S., Canonaco, F., Yao, L., Prévôt, A. S.  
902 H., Petäjä, T., Kulmala, M., Sipilä, M., Worsnop, D. R., and Ehn, M.: Source characterization of  
903 highly oxidized multifunctional compounds in a boreal forest environment using positive matrix  
904 factorization, *Atmos. Chem. Phys.*, 16, 12715-12731, 2016.

905 Yao, L., Garmash, O., Bianchi, F., Zheng, J., Yan, C., Kontkanen, J., Junninen, H., Mazon, S. B.,  
906 Ehn, M., Paasonen, P., Sipilä, M., Wang, M., Wang, X., Xiao, S., Chen, H., Lu, Y., Zhang, B.,  
907 Wang, D., Fu, Q., Geng, F., Li, L., Wang, H., Qiao, L., Yang, X., Chen, J., Kerminen,  
908 V. M., Petäjä, T., Worsnop, D. R., Kulmala, M., and Wang, L.: Atmospheric new particle formation  
909 from sulfuric acid and amines in a Chinese megacity, *Science*, 361, 278-281, 2018.

910

911 Yu, F. and Luo, G.: Simulation of particle size distribution with a global aerosol model:  
912 Contribution of nucleation to aerosol and CCN number concentrations, *Atmospheric Chemistry and*  
913 *Physics*, 9, 7691-7710, 2009.

914

915 Yue, D. L., Hu, M., Zhang, R. Y., Wu, Z. J., Su, H., Wang, Z. B., Peng, J. F., He, L. Y., Huang, X.  
916 F., Gong, Y. G., and Wiedensohler, A.: Potential contribution of new particle formation to cloud  
917 condensation nuclei in Beijing, *Atmos. Environ.*, 45, 6070-6077, 2011.

918

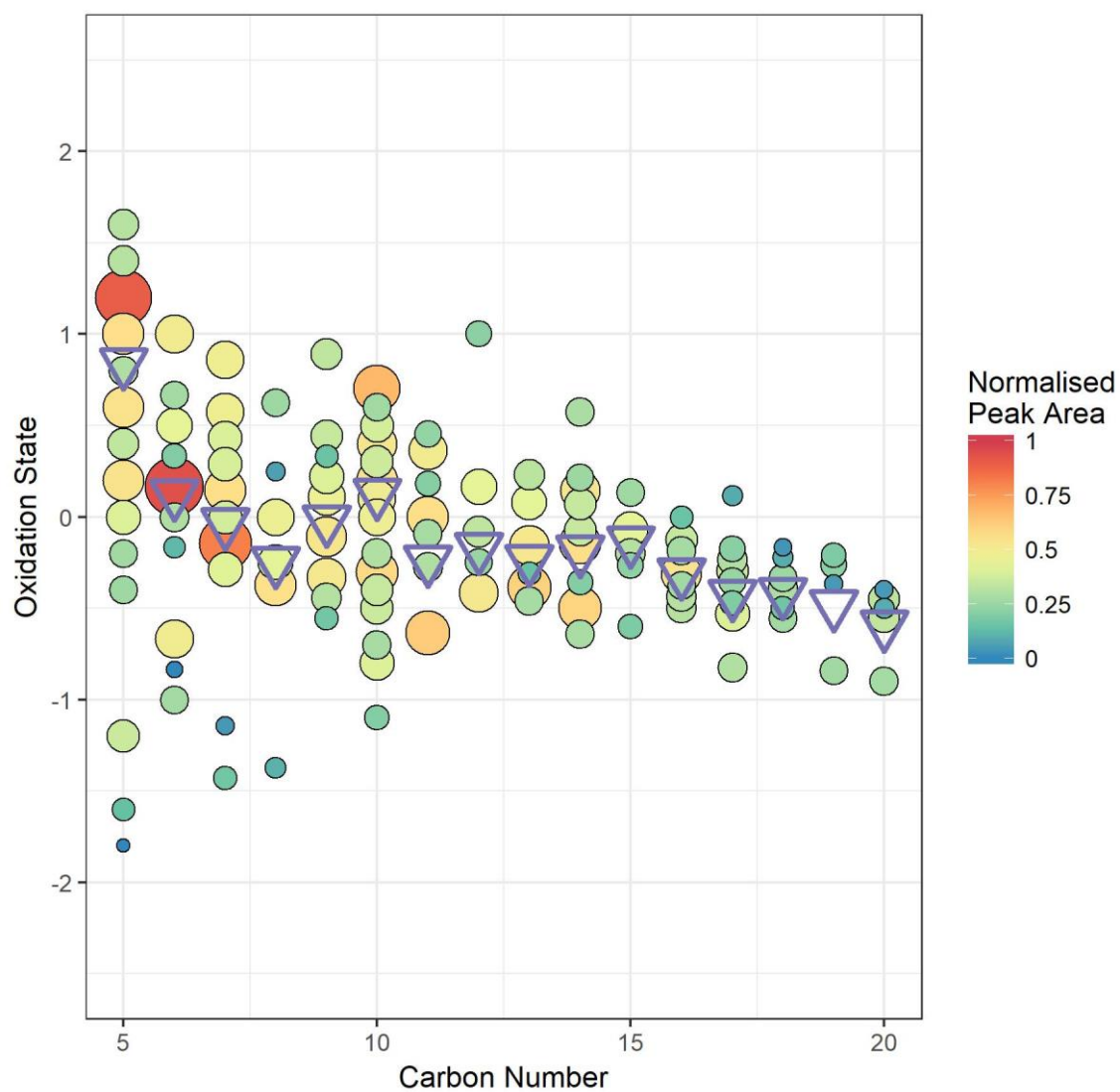
919 Zhao, Y., Wingen, L. M., Perraud, V., Greaves, J., and Finlayson-Pitts, B. J.: Role of the reaction of  
920 stabilized Criegee intermediates with peroxy radicals in particle formation and growth in air, *Phys.*  
921 *Chem. Chem. Phys.*, 17, 12500-12514, 2015.

922

## FIGURE LEGENDS:

- Figure 1** Oxidation state of carbon calculated as two times the oxygen to carbon ratio minus the hydrogen to carbon ratio against carbon number for (colored) individual ions and (blue circles) signal weighted average for each carbon number. Area and colour are both proportional to the peak area for each ion
- Figure 2** Mass defect plot of fitted mass spectral peaks between 100-600 mass units on (a) 10:30 – 12:00 23/06/2017, a non nucleation day, and (b) 10:30 -12:00 25/06/2017, a nucleation day. Mass defect can be defined as the mass - integer mass. The size of point is proportional to the signal intensity. As  $^1\text{H}$  has a positive mass defect (1.007276 Da), the upward trend along the horizontal indicates increasing carbon chain length, and differences at similar masses are due to increasing oxygen functionality, clustering with species such as sulfuric acid (negative mass defect) and ammonia (positive mass defect), as  $^{16}\text{O}$  and  $^{32}\text{S}$  have negative mass defects (15.9949 and 31.9721 Da respectively), while  $^{14}\text{N}$  has a positive mass defect at 14.0031 Da. [The two large peaks seen at 201 and 288 m/Q are the nitrophenol-nitrate cluster and a C<sub>5</sub>H<sub>10</sub>N<sub>2</sub>O<sub>8</sub>-nitrate cluster respectively.](#)
- Figure 3** Summed time series of the [concentrations-normalised signals](#) of (A) all non-nitrogen containing HOMs and all organonitrates identified, (B) C<sub>5</sub>, C<sub>10</sub> and C<sub>20</sub> components, assumed to be dominated by isoprene, monoterpene monomer and monoterpene dimers, signal for C<sub>20</sub> multiplied 50 times to fit scale, and (C) summed C<sub>6</sub> - C<sub>9</sub> components, and summed C<sub>11</sub> - C<sub>18</sub> components, assumed to be dominated by alkylbenzenes and other larger components respectively.
- Figure 4** Time series for the whole sampling campaign for the concentrations of (left axis) VOCs as measured by PTR-ToF and (right axis) a selected HOM product associated with that precursor.
- Figure 5** Normalised unit mass NO<sub>3</sub>- CI-APi-ToF signal intensity on 24/06/2017 (A) and 25/06/2017 (B). Each individual unit mass was normalised to a maximum of 1. Each period is normalised separately so the individual signal maxima on each day are visible. The graph is plotted between 200-600 mass units, with every 10 mass units averaged for simplicity. On the secondary axis is plotted PSM data, both total particle count >1.30 nm (black trace) and total clusters between 1.30 and 1.84 nm (blue trace). Data is plotted at 1 hour time resolution.
- Figure 6** SMPS + PSM contour plot for two nucleation days on 24/06/2017 and 25/06/2017. Data in bottom panel is from the PSM instrument, top panel from NanoSMPS, units in colour bar are  $\log_{10}(\text{dN}/\log D_p)$  for N in  $\text{cm}^{-3}$ . Points signify normalised sulfuric acid concentration (right axis) as measured by CI-APi-ToF.

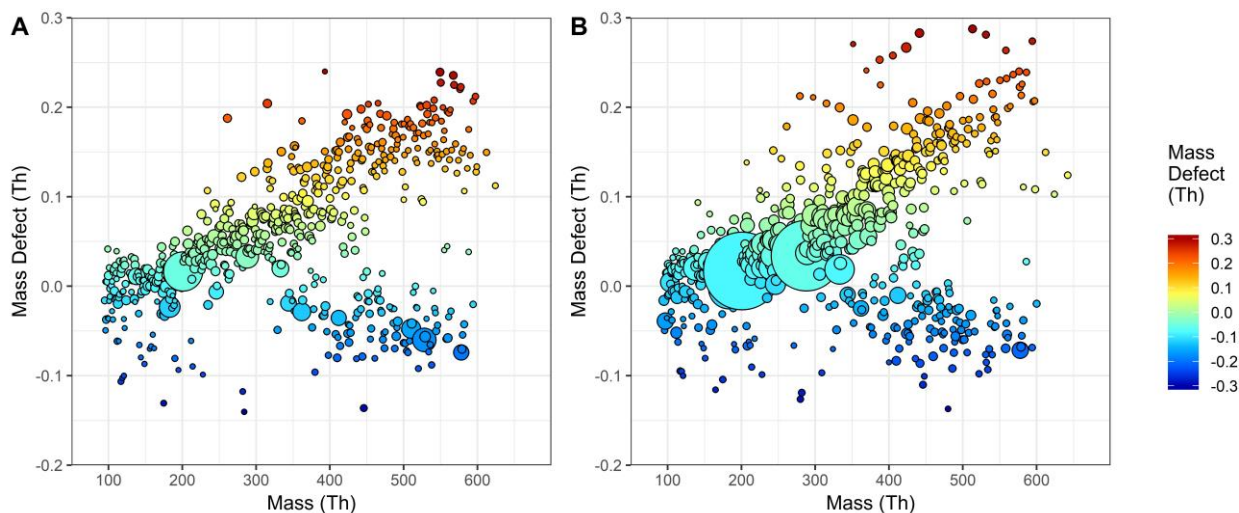
966  
967



968

969 **Figure 1.** Oxidation state of carbon plotted against carbon number for (colored) individual ions and  
970 (purple triangles) signal weighted average for each carbon number. Area and colour are both  
971 proportional to the peak area for each ion.

972

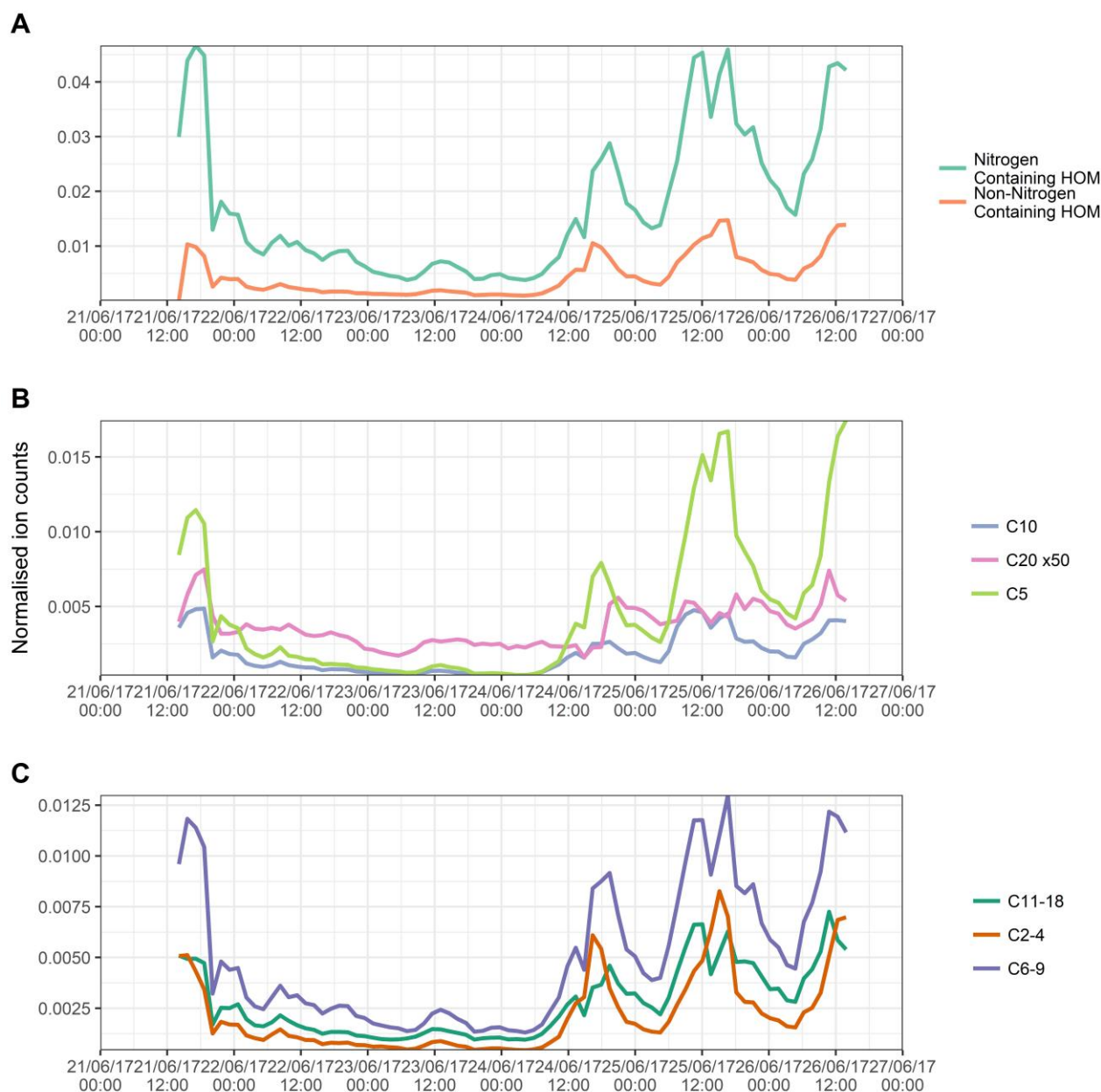


974

975 **Figure 2.** Mass defect plot of fitted mass spectral peaks between 100-600 mass units on (a) 10:30 –  
 976 12:00 23/06/2017, a non nucleation day, and (b) 10:30 -12:00 25/06/2017, a nucleation day. Mass  
 977 defect can be defined as the mass - integer mass. The size of point is proportional to the signal  
 978 intensity. As  $^1\text{H}$  has a positive mass defect (1.007276 Da), the upward trend along the horizontal  
 979 indicates increasing carbon chain length, and differences at similar masses are due to increasing  
 980 oxygen functionality, clustering with species such as sulfuric acid (negative mass defect) and  
 981 ammonia (positive mass defect), as  $^{16}\text{O}$  and  $^{32}\text{S}$  have negative mass defects (15.9949 and 31.9721 Da  
 982 respectively), while  $^{14}\text{N}$  has a positive mass defect at 14.0031 Da. [The two large peaks seen at 201](#)  
 983 [and 288 m/Q are the nitrophenol-nitrate cluster and a  \$\text{C}\_5\text{H}\_{10}\text{N}\_2\text{O}\_8\$ -nitrate cluster respectively.](#)

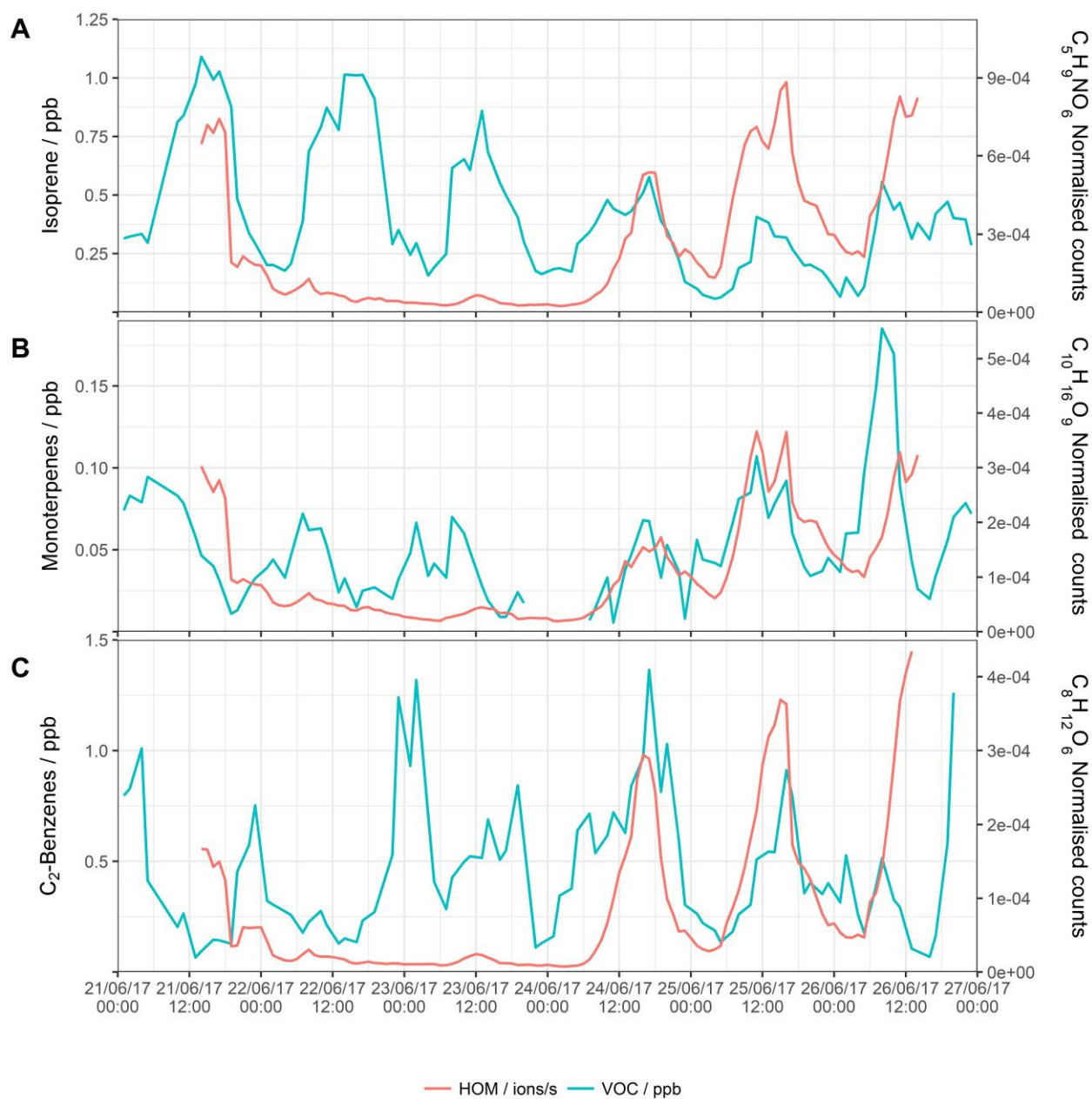
984





985

986 **Figure 3.** Summed time series of the [concentrations-normalised signals](#) of (A) all non-nitrogen  
 987 containing HOMs and all organonitrates identified, (B) C5, C10 and C20 components, assumed to be  
 988 dominated by isoprene, monoterpene monomer and monoterpene dimers, signal for C20 multiplied  
 989 50 times to fit scale, and (C) summed C6 - C9 components, and summed C11 - C18 components,  
 990 assumed to be dominated by alkylbenzenes and other larger components respectively.



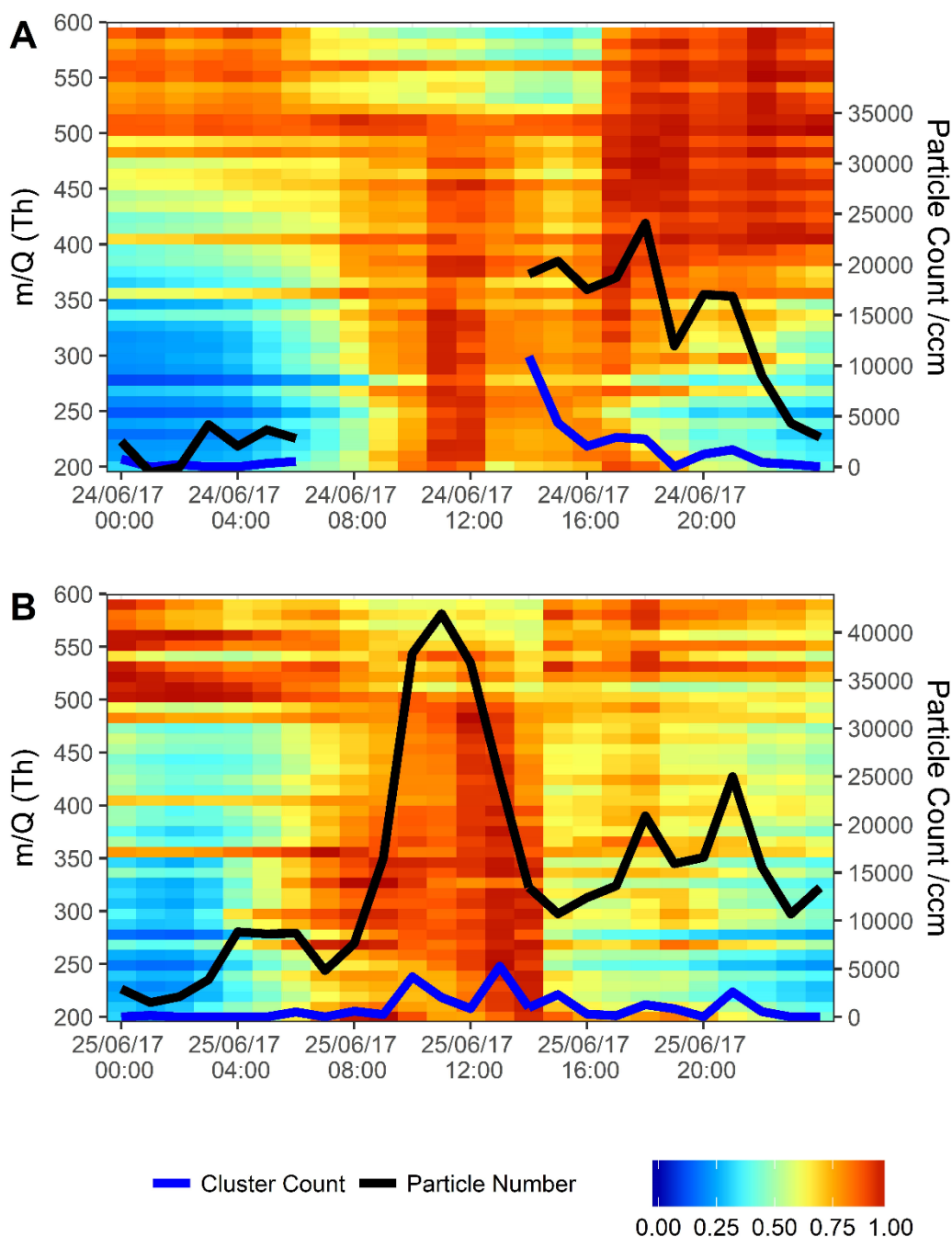
991

992 **Figure 4.** Time series for the whole sampling campaign for the concentrations of (left axis) VOCs as  
 993 measured by PTR-ToF and (right axis) a selected HOM product associated with that precursor.

994

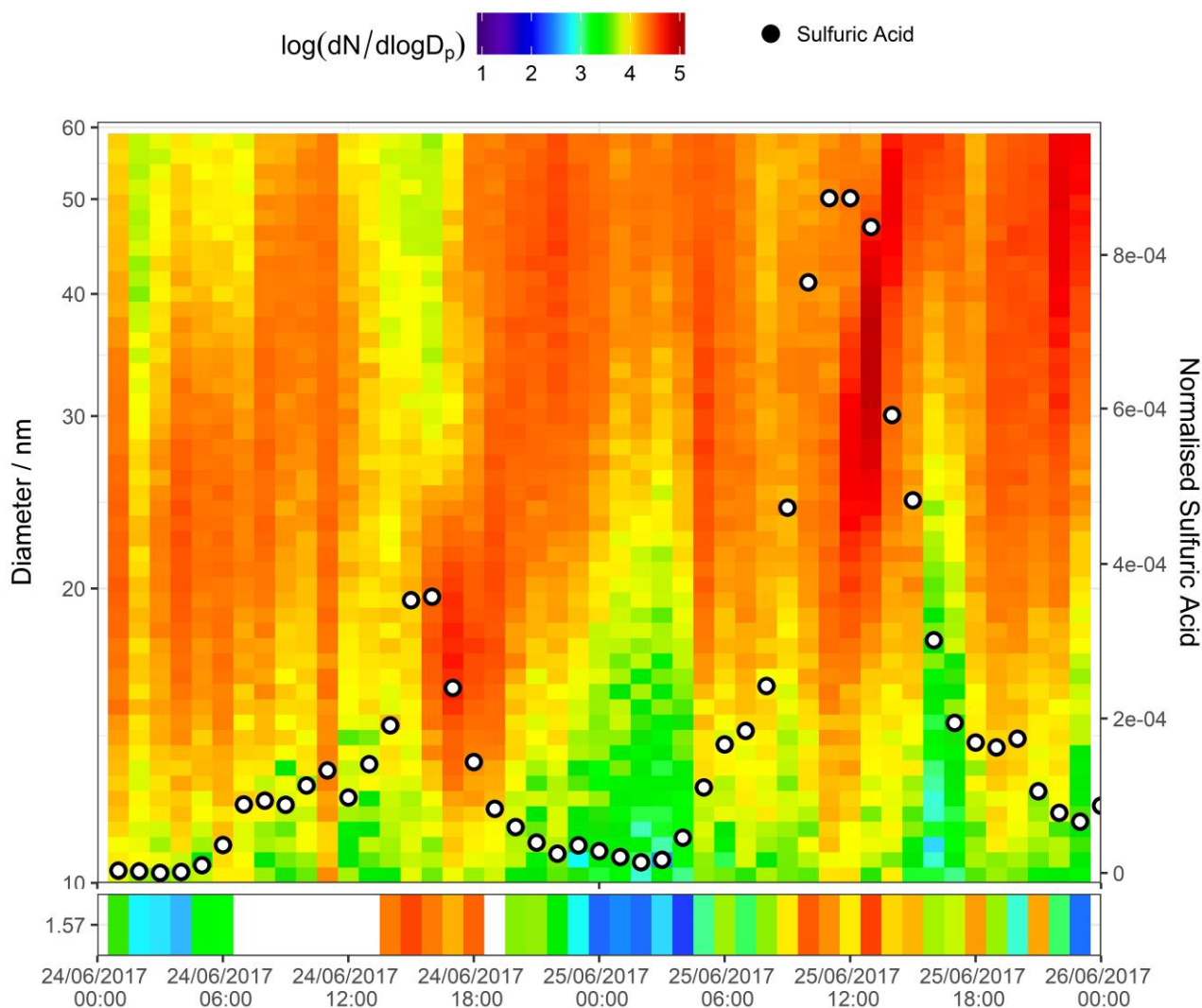
995

996



997

998 **Figure 5.** Normalised unit mass  $\text{NO}_3^-$  CI-APi-ToF signal intensity on 24/06/2017 (A) and 25/06/2017  
 999 (B). Each individual unit mass was normalised to a maximum of 1. Each period is normalised  
 1000 separately so the individual signal maxima on each day are visible. The graph is plotted between 200-  
 1001 600 mass units, with every 10 mass units averaged for simplicity. On the secondary axis is plotted  
 1002 PSM data, both total particle count >1.30 nm (black trace) and total clusters between 1.30 and 1.84  
 1003 nm (blue trace). Data is plotted at 1 hour time resolution.



1004

1005 **Figure 6.** SMPS + PSM contour plot for two nucleation days on 24/06/2017 and 25/06/2017. Data in  
 1006 bottom panel is from the PSM instrument, top panel from NanoSMPS, units in colour bar are  $\log_{10}$   
 1007  $(dN/\log D_p)$  for N in  $\text{cm}^{-3}$ . Points signify normalised sulfuric acid concentration (right axis) as  
 1008 measured by CI-APi-ToF.

1009

1010

1011

1012

1013

1014

1015